

1 Revision 1

Word Count: 9316

2 **Revisiting the genesis of the adakite-like granitoids in collisional**
3 **zones: water-fluxed melting of intermediate to felsic rocks with**
4 **dilution by low Sr/Y phases**

5

6 Yuan-Hui Xie¹, Joshua J. Schwartz², Xiao-Wei Li^{1,*}, Keda Cai^{1,*}, Bader Thomas³, Huan
7 Li⁴, Fang-Yue Wang⁵, Xiao-Bing Zhang⁶, Xuan-Xue Mo¹, Guo-Chen Dong¹

8

9 ¹State Key Laboratory of Geological Processes and Mineral Resources, and School of
10 Earth Sciences and Resources, China University of Geosciences, Beijing 100083, China

11 ²Department of Geological Sciences, California State University Northridge,
12 Northridge, California 91330, USA

13 ³School of Earth and Space Sciences, Peking University, Beijing 100087, China

14 ⁴Key Laboratory of Metallogenic Prediction of Nonferrous Metals and Geological
15 Environment Monitoring, Ministry of Education, Central South University, Changsha
16 410083, China

17 ⁵Ore Deposit and Exploration Centre, Hefei University of Technology, and School of
18 Resources and Environmental Engineering, Hefei University of Technology, Hefei,
19 230009, China

20 ⁶State Key Laboratory of Isotope Geochemistry, Guangzhou Institute of Geochemistry,
21 Chinese Academy of Sciences, Guangzhou 510640, China

22

23 *Corresponding authors: Xiao-Wei Li xwli@cugb.edu.cn; caikd@cugb.edu.cn

24

25

ABSTRACT

26 High Sr/Y granitoids in continental settings are sometimes erroneously regarded as
27 the products derived from partial melting of thickened/delaminated mafic lower crust
28 under relatively higher pressures (> 1.5 GPa) in a collisional orogenic setting. In fact,
29 multiple magmatic processes in the trans-crustal magma system such as recycling of
30 antecrysts, crustal assimilation, and fractional crystallization can create or modify
31 primary ‘adakitic’ signature. As a result, the generation of adakitic magmas in
32 continental settings remains controversial from a bulk-rock perspective. Here, we
33 address the origin of adakitic plutonic rocks through geochemical and textural
34 characterization of rock-forming minerals in the pyroxene-bearing, Zhuyuan
35 granodiorite (West Qinling, China). The Zhuyuan granodiorite formed in a post-
36 collisional setting, and primarily consists of resorbed orthopyroxene, three types of
37 clinopyroxene, amphibole, two types of plagioclases, K-feldspar, biotite, and quartz.
38 Type-1 Cpx has high X_{Mg} (70.0–81.7). Type-2 Cpx displays normal zoning and
39 decreasing X_{Mg} (80.9 to 71.5) from the core to rim. Type-3 Cpx is reversely zoned,
40 where the rims have higher X_{Mg} (75.5–86.9), Ni, Cr, suggesting a recharge event.
41 Orthopyroxene has high Ni and Cr contents, as well as high X_{Mg} (80.9–82.8), indicative
42 of antecrysts that grew in mafic magma reservoirs. The injection of magmas from
43 different sources is supported by sieve-textured plagioclase and crystal size

44 distributions of non-poikilitic amphibole. Finally, non-sieve textured plagioclase,
45 biotite, K-feldspar, and quartz are late-crystallized phases, indicative of an orthocrystic
46 origin. The melts in equilibrium with these orthocrysts display significantly higher Sr/Y
47 values than the magma batches that crystallized other mafic phases (i.e., amphibole,
48 clinopyroxene, and orthopyroxene). Thus, we propose that the system involved an
49 initial high-Sr/Y melts in equilibrium with the orthocryst assemblage were generated
50 by water-fluxed melting of intermediate to felsic sources. The addition of low Sr/Y non-
51 orthocrysts (e.g., amphibole and pyroxene) and associated melt diluted the original
52 ‘adakitic signal’ in the magma reservoir, and drove the bulk composition to more mafic
53 values. Consequently, the Zhuyuan pyroxene-bearing granodiorite represents a mixture
54 of crystals with diverse origins and distinct magma batches of various compositions
55 (from felsic to mafic compositions). Our study emphasizes that the origin of adakitic
56 granitoids cannot be clearly deciphered without the geochemical analysis of the
57 constituent minerals. We also suggest that Sr/Y values in plutons should be cautiously
58 used in paleo-crustal thicknesses estimates in collisional settings because of possible
59 open system scenarios like we document here.

60 **Keywords:** Adakitic rock, antecryst, dilution, pyroxene-bearing granodiorite, water-
61 fluxed melting

62

63

INTRODUCTION

64 The term “adakite” was originally defined as high-Mg andesites produced by partial
65 melting of subducted oceanic crust (Kay, 1978; Defant and Drummond, 1990).
66 Geochemically, adakites are characterized by elevated Sr contents (> 400 ppm), high
67 Sr/Y and La/Yb values, but depleted Y (< 18 ppm) and HREE (e.g., Yb < 1.8 ppm)
68 (Defant and Drummond, 1990). A number of mechanisms have been proposed for the
69 origin of adakitic magmas based on whole-rock geochemical compositions (Ma et al.,
70 2015; Shen et al., 2021 and references therein). For example, primary magmas with
71 adakitic affinity may be generated by partial melting of various sources under various
72 pressures (e.g., delaminated lower crust, thickened lower crust, mantle wedge peridotite
73 metasomatized by slab melts, intermediate to felsic source rocks with initially high Sr,
74 low Y and Yb; Calmus, 2003; Moyen et al. 2009; Ma et al., 2015; Ji et al., 2018; Ou et
75 al., 2017; Yu et al., 2015; Zhan et al., 2020). On the other hand, magma processes (e.g.,
76 fractional crystallization, crystal accumulation and/or magma mixing) may produce or
77 modify ‘adakitic’ felsic melts (e.g., Chen et al., 2016; Guo et al., 2007). For example,
78 amphibole fractionation prior to plagioclase saturation would lead to the enrichment of
79 Sr and depletion of Y in derivative melts (Moyen, 2009; Nandedkhar et al., 2016). As
80 such, the origin of adakites has been controversial and this issue warrants further
81 reevaluation via comprehensive mineral-scale geochemical investigation (Castillo,
82 2012; Castillo et al., 1999).

83 Moreover, previous mechanisms for the generation of adakitic magmas are largely
84 based on experiments and modeling using a simple rock source or a melt-dominated

85 closed system (e.g., Martin et al., 2005; Stern and Kilian, 1996); however, recent crystal
86 population studies regarding trans-crustal magma-mush reservoirs have challenged the
87 suppositions necessary to generate adakitic magmas especially in plutonic arc crust
88 (e.g., Paterson et al., 2016; Graham et al., 2020; Brackman & Schwartz, 2022). For
89 example, some workers argue that felsic magma reservoirs likely comprise multiple
90 generations of crystals (e.g., orthocrysts, antecrysts, peritectic crystals, or xenocrysts;
91 Bach et al., 2012; Miller et al., 2007; Clemens and Stevens, 2012) of contrasting origins
92 (Jerram et al., 2018; Miller et al., 2007), which are entrained by different batches of
93 both interstitial melts and volatile phases (i.e., a system of melt stored in a framework
94 of crystals, referred to as crystal mush; Cashman et al., 2017; Collins et al., 2020;
95 Wieser et al., 2020). In some cases, original adakitic signals (i.e., high Sr/Y and La/Yb
96 values) could be diluted by the addition of non-orthocrysts characterized by low Sr/Y
97 values (e.g., Macpherson et al., 2006), and as a consequence, geochemical trends
98 defined by the whole-rock compositions could deviate from the liquid line of descent
99 of the host magma due to the addition of various proportions of non-orthocrysts.

100 One approach to characterize these complex geochemical signals is to study the
101 composition of individual minerals such as plagioclase, pyroxenes, titanite, zircon, and
102 apatite which have become widely used as petrogenetic tools in supplementing or even
103 replacing conventional bulk-rock analyses. For instance, Hollings et al. (2020) used
104 early-crystallized apatite to show that the ‘adakite signal’ of the equilibrium melt had
105 not been influenced by subsequent amphibole-dominated fractional crystallization. In

106 this regard, geochemical signatures of constituent minerals that witnessed different
107 stages of the geochemical evolution history and/or various sources may provide new
108 perspectives for further constraining mechanisms of adakites generation.

109 Here, we explore the Late Triassic post-collisional granodiorite pluton in the
110 Zhuyuan area, West Qinling which has complex mineral assemblages and show
111 remarkably whole-rock high Sr/Y properties, a diagnostic imprint of adakitic rocks.
112 This makes it a valuable target for exploring the contribution of different generations
113 of minerals to the nature of adakitic granitoids. In this study, we have classified several
114 types of amphiboles, plagioclase and pyroxenes in the Zhuyuan pluton. Multiple lines
115 of evidence support open-system processes including pluton construction from multiple
116 generations of antecrysts and magma batches in a felsic magma reservoir at shallow
117 crustal depths. Furthermore, we argue that water-fluxed melting of intermediate to
118 felsic sources controls the development of high Sr/Y interstitial melts of the studied
119 pluton and it has no tectonic indication for thickened/delaminated mafic lower crust
120 even though emplacement during post-collisional settings.

121

122 **SAMPLE DESCRIPTIONS**

123 The Zhuyuan pluton investigated in this study intruded Devonian strata (the
124 Wangjiaba, Weijiamu, and Yuchiba Formation) in the eastern part of the West Qinling
125 Orogenic Belt (Fig. 1b and 2). All 17 samples are classified as granodiorites (Fig. DR1;
126 Streckeisen, 1976). They display a medium- to fine-grained texture (Fig. 3a–3b). Rock-

127 forming minerals include quartz (Qtz: ~20 vol%), plagioclase (Pl: 40–45 vol%), K-
128 feldspar (Kfs: 15–20 vol%), biotite (Bt: ~5 vol%), amphibole (Amp: 5–10 vol%),
129 clinopyroxene (Cpx: ~5 vol%), and orthopyroxene (Opx: <2 vol%). Accessory minerals
130 are apatite, zircon, titanite, and magnetite.

131 Two types of Pl crystals are identified. One is clear without resorbed cores or
132 oscillatory zoning; it occurs as phenocrysts or microlites in the groundmass, and
133 generally exhibits polysynthetic twinning (Fig. 3b). The other type commonly displays
134 oscillatory zoning with patchy- or sieve-textured cores surrounded by clear rims (Fig.
135 3c–3d). The sieve texture (Fig. 3c) indicates disequilibrium or resorption and thus
136 implies a xenocrystic (Xu et al., 1999) or antecrystic origin (Jerram and Martin, 2008)
137 for the cores. Kfs is anhedral and generally measure less than 1 mm (Fig. 3b).

138 Pyroxenes display poikilitic textures (Fig. 3e–3i), are anhedral to subhedral, and have
139 sizes of 0.05–1 mm in length. All Cpx and Opx with ragged margins are enclosed by
140 Amp, reflecting the formation of Amp at the expense of pyroxene (Fig. 3e–3i). Based
141 on back-scattered electron (BSE) images and geochemical characteristics, we identify
142 three types of Cpx: unzoned (Type-1 Cpx), normally zoned (Type-2 Cpx), and reversely
143 zoned (Type-3 Cpx) crystals. In BSE images, both Type-2 and Type-3 Cpx (Fig. 3g)
144 show zoning with core–rim textures, while Opx does not display zoning (Fig. 3i).

145 Amp is one of the principal mineral phases in the Zhuyuan granodiorites that
146 occasionally forms aggregates. Amps are euhedral to subhedral, with sizes of 0.01–2.5
147 mm in diameter, have distinct brown to pale green pleochroism, and do not display

148 zoning in BSE images (Fig. 3g). Some Amps display poikilitic textures with Bt (Fig.
149 3c). According to the texture and particle sizes, we divided them into two types (Type-
150 1 Amp and Type-2 Amp). Type-1 Amp grows along pyroxene grain boundaries and
151 forms a poikilitic texture with pyroxene. Their size is greater than 0.3 mm. Type-2 Amp
152 does not show poikilitic textures with pyroxene and has smaller grain sizes (0.01–0.4
153 mm). Most Amps occur as corroded grains and do not display equilibrium grain
154 boundary textures where they are in contact with Pl and they generally exhibit lobate
155 textures (Fig. 3g–3i). This observation suggests that Amp and Pl do not exist in the
156 same equilibrium mineral assemblage. Subhedral to anhedral Bts are khaki to brown,
157 with a length of less than 1 mm. Bts usually occurs as interstitial phases associated with
158 Kfs and Qtz.

159

160

RESULTS

161 Mineral element compositions

162 Representative in-situ major- and trace-element data of Opx, Cpx, Amp, Bt, Pl, and
163 Kfs from the Zhuyuan granodiorites are listed in Tables DR3–DR4 and shown in Fig.
164 4 to 6. In order to ensure the reliability of the data, we only use trace element
165 concentrations higher than 0.1 ppm (generally 5 greater than times the detection limit)
166 for interpretations and calculations. Chemical formulae for Bt and Pl were calculated
167 with the AX software (Holland and Blundy, 1994). For pyroxene, we use the Geokit
168 software (Lu, 2005), and for Amp we use the method proposed by Li et al. (2020a).

169 To determine trace-element distributions in mineral phases, several mineral grains
170 were selected for LA-ICP-MS element mapping. A total of 51 elements were mapped
171 for these minerals, and Fig. 7–9 display the elements of interest (i.e., Al, Sr, Y, REE,
172 Cr, and Ni) and important parameters (Sr/Y and X_{Mg} values). Fig. 7 and Fig. 9 present
173 compositional profiles across core-rim interfaces, and Tables DR4 contain the
174 corresponding data.

175 **Clinopyroxene** shows a large range of SiO_2 (50.0–54.1 wt.%) and MgO (12.4–17.1
176 wt.%) contents, high X_{Mg} ($Mg/[Mg + Fe^{2+}] \times 100$) of 70.0–86.9, and variable $\Sigma REEs$
177 (37.8–245 ppm), Cr (145–5821 ppm), and Ni (56.2–346 ppm) abundances (Tables 1
178 and DR4). All are classified as diopside or augite (Fig. 4a). Several grains exhibit
179 compositional zonation (Fig. 5). By observing BSE images and geochemical data, we
180 identified three types of Cpx (Fig. 5): unzoned, normally zoned, and reversely zoned.

181 Unzoned Cpxs (Type-1 Cpx) are subhedral to anhedral and compositionally are
182 diopside and augite (Fig. 4a). We further divide them (Type-1A and Type-1B) based
183 on their FeO^T contents, X_{Mg} values, and chondrite-normalized REE patterns, and both
184 subtypes may occur in a single thin section. Type-1A Cpx is characterized by high X_{Mg}
185 (72.6–81.7; Fig. 5a), variable FeO^T (6.63–9.69 wt.%), and low $\Sigma REEs$ (54.3–75.0 ppm;
186 Tables DR3–DR4). They have chondrite normalized REE distribution patterns with
187 negative slopes and moderately negative Eu anomalies ($Eu/Eu^* = 0.54–0.68$) (Fig. 6a).
188 The primitive mantle-normalized trace element patterns (Fig. 6b) show depletions in
189 Sr, P, Nb, Ta, Zr, Hf, and Ti, and enrichments in Pr, Nd, and Sm.

190 Type-1B Cpx has higher FeO^{T} (9.67–11.0 wt.%), Cr (551–1033 ppm), Ni (185–187
191 ppm), and ΣREEs (135–189 ppm) but slightly lower X_{Mg} (70.0–76.5; Fig. 5b, Table 1)
192 than Type-1A Cpx. In addition, the Type-1B Cpx exhibit moderately negative Eu
193 anomalies ($\text{Eu}/\text{Eu}^* = 0.41\text{--}0.43$, Fig. 6a). The primitive mantle-normalized trace
194 element patterns (Fig. 6b) of both sub-types are similar.

195 Normally zoned Cpx is subhedral, with slightly darker cores and brighter rims (Fig.
196 5c–5d). The cores exhibit high X_{Mg} (76.1–80.9; Fig. 5d, Table 1) and Cr contents
197 (1210–1377 ppm) but low ΣREEs (53.7–60.9 ppm). Their chondrite-normalized REEs
198 (Fig. 6c) display weakly negative Eu anomalies ($\text{Eu}/\text{Eu}^* = 0.73\text{--}0.78$). The Type-2 Cpx
199 cores show significant depletions in HFSEs (e.g., Nb, Ta, Zr, Hf, and Ti), K, and P and
200 enrichments in Pb and Nd (Fig. 6d). In comparison with the Type-2 Cpx cores, their
201 rims have slightly higher FeO^{T} (8.75–9.92 wt.%) and ΣREEs (139–245 ppm), but lower
202 MgO (12.4–14.6 wt.%) contents and X_{Mg} (71.5–76.2). In addition, the Type-2 Cpx rims
203 have much stronger negative Eu anomalies ($\text{Eu}/\text{Eu}^* = 0.32\text{--}0.46$, Fig. 6c) and larger
204 ranges of the Nb, Ta, and K concentrations (Fig. 6d).

205 Reversely zoned Cpx (Type-3 Cpx) is subhedral with brighter cores and darker rims
206 in BSE images (Fig. 5e–5f). The bright cores contain 14.3–16.0 wt.% of MgO with X_{Mg}
207 of 74.3–83.2, are classified as diopside and augite with $\text{Wo} = 41.8\text{--}46.5$ mol% (Fig.
208 4a), have slight negative Eu anomalies ($\text{Eu}/\text{Eu}^* = 0.82\text{--}0.97$; Fig. 6e). As revealed by
209 primitive mantle-normalized trace element patterns, rims of the Type-3 Cpx show
210 depletions in HFSEs (e.g., Nb, Ta, Zr, Hf, and Ti), Ba, K, and P but enrichments in Nd,

211 Th, and Pb (Fig. 6f). By contrast, the dark rims contain slightly more MgO (14.6–17.1
212 wt.%) with X_{Mg} of 75.5–86.9 (Fig. 5f, Table 1), are augite with a lower Wo content
213 (42.1–44.1mol%). The BSE darker rims show similar primitive mantle-normalized
214 trace element patterns as the bright cores (Fig. 6e), but significantly higher Cr (3480–
215 5821 ppm) and Ni (244–346 ppm) contents.

216 One Type-3 Cpx from sample ZY17-4 was selected for LA-ICP-MS element
217 mapping. The Cr and Ni concentrations are higher in the rim than in the core (Fig.7),
218 likely reflecting a mafic magma recharge event. Element data of the corresponding
219 cross-section (Profile A) are provided in Table DR4. The Cr contents are lower in the
220 core (530–1500 ppm), but higher in the rim (2315–10375 ppm), which also applies to
221 Th and Sr, resulting in higher Sr/Y values in the rim (core: 4.45–9.49, rim: 5.85–18.5;
222 Table DR4).

223 **Orthopyroxene** are classified as enstatite (Fig. 4a) with a compositional range of
224 $Wo_{2.02-2.58}En_{78.9-80.9}Fs_{17.1-19.0}$. They have high Cr (1854–2261 ppm) and Ni (591–837
225 ppm) concentrations, high X_{Mg} of 80.9–82.8, and low abundances of Al_2O_3 (1.76–2.86
226 wt.%), TiO_2 (0.09–0.18 wt.%), and CaO (1.01–1.30 wt.%; Xie et al., 2023), and very
227 low $\Sigma REEs$ (0.73–2.82 ppm; Table DR4).

228 On a LA-ICP-MS element map of one representative Opx of sample ZY17-15 (Fig.
229 8), the crystal shows a ubiquitous enrichment of Cr and Ni. Notably, the Sr/Y values
230 increase significantly along the cleavage, cracks, and edges of this crystal, probably
231 reflecting the influence of late-stage magmatic/hydrothermal activity.

232 **Amphibole.** Using the amphibole nomenclature and classification schemes of Leake
233 et al. (1997) and Li et al. (2020a), all the analyzed Amps are calcic ($\text{Ca}_B \geq 1.5$ atoms per
234 formula unit, $(\text{Na} + \text{K})_A < 0.5$ atoms per formula unit) and are classified as
235 magnesiohornblende (Fig. 4b). There are no obvious compositional differences
236 between larger (Type-1 Amp) and smaller (Type-2 Amp) Amps (Table DR3–DR4).
237 They feature variable SiO_2 (46.5–51.0 wt.%), Cr (77–1038 ppm), and Ni (103–205
238 ppm) contents, moderately high X_{Mg} (63.1–74.6), and limited ranges in Al_2O_3 (4.22–
239 6.14 wt.%), TiO_2 (0.48–1.21 wt.%), and total alkalis ($\text{Na}_2\text{O} + \text{K}_2\text{O}$: 1.11–1.79 wt.%).
240 The Amps show high $\sum\text{REEs}$ (303–712 ppm), pronounced negative Eu anomalies
241 ($\text{Eu}/\text{Eu}^* = 0.14\text{--}0.29$) and obvious depletion of HREE relative to LREE (Fig. 6g). They
242 are depleted in Ba, Sr, and Zr, but enriched in Nd and Sm (Fig. 6h).

243 LA-ICP-MS element mapping of one magnesiohornblende (Type-2 Amp) abutting
244 Opx (Fig. 8) confirms the compositional features (e.g., relatively high X_{Mg} and low
245 Sr/Y) of the single spot in-situ analysis.

246 **Biotite** exhibit relatively consistent Al^{IV} values (1.13 a.p.f.u. to 1.32 a.p.f.u.) and
247 contain high FeO^{T} (19.1–20.6 wt.%) and Al_2O_3 (12.7–14.6 wt.%) and moderate MgO
248 (11.1–14.3 wt.%); X_{Mg} are 54.4–61.5 (Table 1). According to the classification of
249 Foster (1960), the Bts are within the compositional range of magnesian biotite (Fig. 4c).
250 Nachit et al. (2005) discriminate magmatic or primary biotite from secondary or re-
251 equilibrated primary biotite in a $10 \times \text{TiO}_2\text{--FeO}^*(= \text{FeO} + \text{MnO})\text{--MgO}$ ternary diagram
252 (Fig. 4d). On this diagram, all analyzed Bts plot in the primary biotite field. The trace

253 element compositions of the Bts vary slightly (Table DR4): they have low abundances
254 of Sr (1.74–6.74 ppm), relatively low concentrations of Y (0.15–0.33 ppm), with high
255 values of Sr/Y (17.5–43.8), relatively low Σ REEs (ranging from 0.30 to 4.12 ppm),
256 relatively high contents of Rb (317–601 ppm), Ba (471–6055 ppm), Nb (27.5–53.7
257 ppm), and Ni (191–283 ppm), but low abundances of Ta (1.00–4.79 ppm) and Hf (0.12–
258 0.28 ppm).

259 One Bt from sample ZY17-4 was selected for LA-ICP-MS element mapping (Fig. 9)
260 and acquisition of one cross-section (Profile B; Table DR4). The core of this Bt features
261 lower Sr, Cu, and Pb concentrations than the rim. The entire Bt shows high Sr/Y values
262 (7.32–174), relatively high X_{Mg} values (52.1–60.1), and high abundances of Ni (307–
263 459 ppm), Ba (2840–6438 ppm), and Rb (191–382 ppm). All these characteristics are
264 similar to those of the Bts described above based on single spot in-situ analysis.

265 **Plagioclase** are mainly classified as oligoclase–andesine and subordinately as
266 labradorite (Fig. 4e), with anorthite contents (An) of 14.9–51.6 mol-% (Tables 1 and
267 DR3–DR4). We identify two distinct Pl populations: sieve-textured Pl cores (Type-1
268 Pl) with rim overgrowths (Fig. 5g), and unreacted Pls devoid of sieve textures (Type-2
269 Pl, Fig. 5h). The sieve-textured Pl cores (Type-1 Pl) exhibit higher An (32.9–51.6
270 mol-%) and Rb contents (10.4–318 ppm) than their overgrowth rims (Type-2 Pl; 15.6–
271 29.4 mol-% and 0.92 ppm, respectively; Table 1). Type-2 Pls are homogeneous in
272 composition, and contain low An (14.9–26.9 mol-%) and Rb (0.31–4.28 ppm; Table 1).
273 The composition of the sieve-textured Pl rims is similar to that of the Type-2 Pl, we

274 therefore propose both of them grew at the same time. In other words, we consider the
275 rims on Type-1 grains as part of the same geochemical group (Type-2 Pl). Both types
276 of Pls have variable Σ REEs abundances (12.8–45.3 ppm), high Sr (865–1519) ppm but
277 extremely low Y contents (0.10–0.22 ppm), and high Sr/Y (4254–14513) (Table 1).

278 LA-ICP-MS element mapping of several Pl inclusions within the Amp featured in
279 Fig. 8 shows that Pls have high Sr contents (\sim 66.9–1860 ppm) and high Sr/Y (\sim 25.3
280 to 62600) and Sr/Rb (\sim 17.0 to 66200) values, similar to Type-2 Pls and sieve-textured
281 Pl rims described above. This indicates that the appearance of these Pls included by
282 Amp might be the result of the sectioning-effect (Pls protruding into Amp from the top
283 or bottom of the thin section), and these Pls do not crystallize earlier than hornblende.
284 The similar sectioning-effect also occur between Amp and pyroxene (Fig. 7).

285 It should be noted that HREE are sometimes close to or below the detection limits in
286 Pl, and the extremely high Sr/Y values of some Pl crystals are not accurate.

287 **K-feldspars** are sanidine, and their orthoclase (Or) contents range from 72.4 to 95.8
288 mol-% (Table DR3). They display very high positive Eu anomalies ($\text{Eu}/\text{Eu}^* > 4.01$,
289 Tables 1 and DR4), high concentrations of Rb (197–338 ppm), Ba (1077–5925 ppm),
290 and Sr (535–1029 ppm), low contents of Y (≤ 0.1 ppm, the Y contents of several crystals
291 are below the detection limit), with correspondingly extremely high Sr/Y values ($>$
292 5345; Table 1).

293

294 **Crystal size distribution (CSD)**

295 We analyzed a 354 mm² area across two thin sections and observed 2246 Amp with
296 non-poikilitic textures covering an area of 41.4 mm² (see Table DR5 for CSD analysis
297 data of these Amps). The crystal sizes range from 0.01 mm to 0.4 mm (Fig. 10a–10b).
298 On a plot of the logarithm of the crystal population density ($\ln(n)$) versus size (L) (Fig.
299 10c–10d), the CSDs of both samples exhibit a significant change in slope, from a
300 shallow gradient in the larger crystals to a steeper gradient in the smaller crystals. As
301 shown in Fig. 10 the Amp CSD may be separated into at least two groups, and the
302 regression curve equations of different groups of Amp CSDs are given in the figure.
303 Linear CSD curves generally indicate that the crystal population densities are primarily
304 controlled by crystal nucleation and growth, whereas kinked CSDs are usually
305 explained by the mixing of different crystal generations (Burney et al., 2020; Higgins,
306 1996; Morgan et al., 2007; Wang et al., 2019; Yang et al., 2010).

307

308 **DISCUSSION**

309 A key problem in interpreting adakitic rocks in continental settings is that felsic
310 magmatic rocks commonly represent an assembly of interstitial melts and several
311 crystal populations with different origins (Namur et al., 2020 and references therein).
312 In the case of the Zhuyuan granodiorites, we also hypothesize that their high-Sr/Y signal
313 could be derived from multiple batches of magmas within an open magmatic system.
314 We combine whole-rock geochemical characteristics with in-situ mineral compositions
315 to highlight the potential role of magma mixing in the formation of the Zhuyuan

316 granodiorites. The relevant discussion is provided in the "Supplementary Materials".
317 Furthermore, in subsequent discussions, we focus on the origin and evolutionary
318 process of the high-Sr/Y signature of the Zhuyuan granodiorites.

319

320 **Crystal–melt equilibria**

321 Assuming that the minerals were in equilibrium with the corresponding host melts
322 during crystallization, the geochemical compositions of the parental magmas may be
323 estimated with compositionally appropriate mineral-melt partition coefficients (K_D ;
324 Table DR6). Based on petrographic observations (Fig. 3), we have determined the
325 complex mineral associations of the Zhuyuan granodiorites, which is mainly composed
326 of 11 kinds of minerals, including three types of Cpxs, Opx, two types of Amps, two
327 types of Pls, Bt, Kfs and Qtz. Because there is no difference in compositional
328 characteristics and crystallization conditions between the Type 1 Amp and Type-2 Amp
329 (Tables DR3–DR4), we consider them to have formed in the same trans-crustal
330 magmatic system. In addition, Bt, Kfs, and Qtz are the interstitial minerals, and are the
331 most easily identifiable late-stage crystalline mineral phases, which could have possibly
332 formed in the same magmatic environment. Thus, we provisionally define eight magma
333 environments (A, B, C, D, E, F, G, and H) in which different types of minerals
334 crystallized (Table 2). Based on the mineralogical characteristics, we initially classified
335 the magmatic environments into four subtypes: A-D, E, F-G, and H. In the following,
336 these magma environments could be identical, similar, or distinct. We will further

337 discuss the significance of these below in Section ‘Crystal cargoes in the magmatic
338 plumbing system’

339 1. Environments A, B, C, and D: the parental magmas, in which the various types of
340 pyroxenes crystallized

341 We use the Fe–Mg exchange coefficient ($K_D(\text{Fe–Mg})^{\text{Cpx–liq}}$) value of 0.27 ± 0.03 to
342 calculate the Mg# of melts in equilibrium with Cpxs (Pichavant and Macdonald, 2007;
343 Putirka, 2008; Sisson and Grove, 1993). Considering the high X_{Mg} of pyroxenes in this
344 study, we use partition coefficients between pyroxene and basaltic melts to calculate
345 trace-element compositions of the melt in equilibrium with the pyroxene (Bédard, 2001;
346 Elkins et al., 2008). Calculated trace-element concentrations of melts in equilibrium
347 with pyroxenes are listed in Tables 2 and DR6.

348 The calculated equilibrium melts (Environment A) of the Type-1 Cpx have a wide
349 range of Mg# (39.5–55.5) and values of Type-1A (39.5–47.7) and Type-1B Cpx (42.7–
350 55.5) overlap. Melts in equilibrium with Type-1A Cpx exhibit moderately negative Eu
351 anomalies ($\text{Eu}/\text{Eu}^* = 0.54\text{--}0.68$; Fig. 11a), relatively high Ce/Pb values (83.6 on
352 average), and low Sr/Y values (4.52–7.27) (Fig. 12). Type-1B Cpx equilibrium melts
353 have more pronounced negative Eu anomalies ($\text{Eu}/\text{Eu}^* = 0.41\text{--}0.43$), comparable
354 Ce/Pb values (78.8–156), and lower Sr/Y values (1.97–2.57). Type-1A and Type-1B
355 Cpx equilibrium melts show similar chondrite-normalized rare earth element
356 distribution patterns.

357 The melts (Environment B) in equilibrium with Type-2 Cpx have Mg# of 41.3 to
358 54.2. The melts in equilibrium with Type-2 Cpx cores display slight to moderate Eu
359 anomalies ($\text{Eu}/\text{Eu}^* = 0.72\text{--}0.77$; Fig. 11b) and low Sr/Y (11.3–12.2) but high Ce/Pb
360 values (15.5 on average). Compared with the cores, the melts in equilibrium with Type-
361 2 Cpx rims exhibit more significant negative Eu anomalies ($\text{Eu}/\text{Eu}^* = 0.32\text{--}0.46$),
362 higher ΣREE contents and Ce/Pb values (41.2–133), but lower values of Sr/Y (1.97–
363 3.93).

364 The melts (Environment C) in equilibrium with Type-3 Cpx span a large range of
365 Mg#. The melts in equilibrium with Type-3 Cpx core have Mg# of 44.7–58.1, high
366 Ce/Pb (23.9–55.7) and Sr/Y (17.0–47.6) values, and slight to negligible negative Eu
367 anomalies ($\text{Eu}/\text{Eu}^* = 0.82\text{--}0.96$; Fig. 11c). Compared with the cores, the melts in
368 equilibrium with Type-3 Cpx rim have on average higher Mg# (48.4–65.0), high Sr/Y
369 (37.6–42.4, Fig. 12a) and Ce/Pb values (12.1 on average, Fig. 12b), and negative Eu
370 anomalies ($\text{Eu}/\text{Eu}^* = 0.85\text{--}1.02$). The melts (Environment D) in equilibrium with Opx
371 have high Mg# of 56.8–59.9 ($K_d = 0.31$; Price et al., 2012), high mean Ce/Pb values of
372 11.4 (Fig. 12b), but moderate Sr/Y values (11.7–21.8).

373 2. Environment E: the parental magmas in which two types of Amps crystallized

374 Amp–liquid partition coefficients for trace elements were calculated using mineral
375 composition model proposed by Humphreys et al. (2019) and Shimizu et al. (2017).
376 The melts in equilibrium with Amp (Tables 2 and DR6) feature low Mg# (21.7–34.6),

377 negative Eu anomalies ($\text{Eu}/\text{Eu}^* = 0.13\text{--}0.29$; Fig. 11d), and relatively low Sr/Y (4.13–
378 21.6), and medium Ce/Pb values (8.92 on average).

379 3. Environments F and G: the parental magmas in which both sieve-textured and clear
380 Pl crystallized

381 The partition coefficients of Sr between plagioclase and silicate melts depends on the
382 chemical composition of plagioclase (Bindeman et al., 1998). Plagioclase–silicate melt
383 partition coefficients for Sr, Rb and REE were calculated using mineral composition
384 model proposed by Sun et al. (2017). Partition coefficients for Y and Ba are from Nash
385 (1985). The melts (Environment F) in equilibrium with Type-1 Pl have relatively high
386 Sr/Y (218–315) and Sr/Ba values (0.4–1.27), low Sr/Rb (0.2–6.81) and Ce/Pb (3.18–
387 5.59), and positive Eu anomalies ($\text{Eu}/\text{Eu}^* = 5.44\text{--}8.16$; Table 2). By contrast, the melts
388 in equilibrium with Type-2 Pl (Environment G) display lower Ce/Pb (1.55–2.27),
389 higher Sr/Rb (26.4–252) and Sr/Ba values (0.99–1.67), the same high Sr/Y values
390 (96.5–375), and more obvious positive Eu anomalies ($\text{Eu}/\text{Eu}^* = 4.85\text{--}25.4$).

391 4. Environment H: the parental magmas in which Bt, Kfs, and Qtz crystallized

392 Bt and Kfs mainly appear as interstitial minerals, which are the products of late-stage
393 melt. Therefore, we select the partition coefficients of trace elements for melts in
394 equilibrium with Bt and Kfs refer to studies on silicic magmas (Nash, 1985; Sun et al.,
395 2017; Schnetzler and Philpotts 1970; Ewart and Griffin 1994). The Y content in the
396 analyzed Kfs samples is all lower than 0.1 ppm. Here, we assume 0.1 ppm Y to calculate
397 the Y content of equilibrium melt. The actual content will be much lower than the

398 calculated value, but this does not affect the subsequent discussion. The melts in
399 equilibrium with Bt have high Sr/Y (49.5–124) but low Ce/Pb values (0.01–0.07; Table
400 2). The melts in equilibrium with Kfs are characterized by high Sr/Y values ($\gg 29$),
401 low Ce/Pb values (0.05–0.84) and variable Eu contents (0.35–1.47 ppm; Table 2).

402

403 **Crystallization Conditions**

404 The temperature and pressure of the magma reservoir is essential for our
405 understanding of the origin of different minerals (Blundy & Cashman, 2008).
406 Experimental petrology studies have shown that the Cpx and Amp are sensitive to
407 temperature and pressure during crystallization. Thus, thermobarometers based on
408 compositions of Cpx or Amp are commonly used to estimate the physical conditions of
409 magma reservoirs (e.g., Higgins et al., 2022, Neave et al., 2019, Neave & Putirka, 2017,
410 Putirka, 2016, Putirka, 2008). We chose the thermometer (Eq. 32d in Putirka et al.,
411 2008) and the barometer (Eq. 32a in Putirka et al., 2008) based on Cpx compositions
412 only to estimate the crystallization temperatures and pressures. The thermobarometer
413 we used produces one standard error of estimate (1se) of ± 58 °C and ± 0.31 GPa,
414 respectively (Putirka et al., 2008). Due to the poikilitic textures and the irregular
415 corrosion boundary between pyroxene and Amp, the thermochemical reactions at/near
416 the pyroxene-Amp boundary is significant. It may lead to a large error in conditions
417 with the pyroxene compositions close to the reaction boundary, so we only selected the
418 spot analyses away from the boundary for the corresponding calculation (Table 3).

419 The estimate temperature based on Type-1, Type-2 and Type-3 Cpx range from
420 1150°C to 1191°C, 1130°C to 1192°C and 1173°C to 1211°C, respectively. Estimated
421 pressures vary from 0.48 to 0.75 GPa, 0.4 to 0.84 GPa and 0.38 to 0.61 GPa,
422 respectively. These values correspond to crystallization depths of 18.1–28.4 km, 15.3–
423 31.7 km and 14.2–23.0 km, respectively, indicating that Type-1 and Type-2 Cpx
424 crystallized in magma reservoirs at approximately similar depths, while the Type-3 Cpx
425 formed at shallower crustal levels.

426 In addition, we use the single-phase Amp thermobarometer in Higgins et al. (2022)
427 for determining the crystallization conditions of both types of Amps in this study, which
428 is calibrated using random forest machine learning. The random forest machine learning
429 algorithm can recover subtle non-linear relationships between phase compositions,
430 pressure, and temperature (Higgins et al., 2022). Therefore, this approach is superior
431 for retrieving the physical conditions of Amp formation in open magmatic systems. The
432 temperatures calculated from Amp compositions of the Zhuyuan granodiorites range
433 from 744 ± 38 °C to 814 ± 54 °C. The pressure of Amp crystallization varies from 0.2
434 ± 0.02 GPa to 0.35 ± 0.18 GPa, corresponding crystallization depth ranges from 7.64
435 to 13.4 km. The specific calculation results are listed in Tables 2 and DR3.

436 The Ti-in-zircon thermometer has become an accurate and precise monitor of both
437 igneous and metamorphic thermal history (Bloch et al., 2022, Fu et al., 2008, Schiller
438 & Finger, 2019, Watson et al., 2006). Apparent temperatures for zircon crystallization
439 for the Zhuyuan granodiorites were calculated using the Ti-in-zircon thermometer

440 (Watson et al., 2006). We estimated the apparent peak temperature for the zircons from
441 the Zhuyuan granodiorites (Xie et al., 2023), ranging from 721°C to 787°C (30 zircons;
442 Table DR2). In addition, some of higher apparent temperatures range from 893°C to
443 989°C (3 zircons).

444 The zircons from the Zhuyuan granodiorite show obvious negative Eu anomalies
445 (0.01–0.64, Table DR2; Xie et al., 2023), indicating that they crystallized later than
446 plagioclase or contemporaneously with plagioclase. Considering that Type-2 Pl belongs
447 to the late-stage mineral assemblage, it is reasonable to assume that the crystallization
448 temperatures of Type-2 Pl are close to, or overlapping with, those of zircons. The water
449 contents of the magma (Table DR3), from which the Type-2 Pl crystallized, are
450 calculated using the plagioclase–liquid hygrometer of Waters and Lange (2015), for
451 which the impact of the pressure is negligible but the effect of the temperature is
452 significant (Lange et al., 2009; Waters and Lange, 2015). We have used the whole-rock
453 compositions of our samples as proxies for the primitive melt compositions. However,
454 the hygrometer we employed is insensitive to variations in liquid compositions, and is
455 thus well suited for our samples that have undergone an open-system crustal evolution.
456 Assuming the maximum apparent temperatures for zircon crystallization, we calculate
457 magmatic water contents ranging from 6.12–6.46 wt.% based on rims of Pl with sieve
458 texture and values ranging from 6.11–6.50 wt.% for the Type-2 Pl. Assuming the
459 minimum zircon crystallization temperatures yield values of 7.99–8.34 wt.% for rims
460 of Pl with sieve textures, and 7.99–8.38 wt.% for Type-2 Pl. Consequently, we conclude

461 that the high Sr/Y magma reservoir was hydrous (H_2O contents > 4 wt.%; Patiño Douce,
462 1999; Collins et al., 2020) when late-stage Pl (Type-2 Pl) crystallized.

463

464 **Crystal cargoes in the magmatic plumbing system**

465 Based on the crystallization conditions of different minerals in the Zhuyan pluton
466 and the compositions of equilibrium melts, we attempted to construct an open magmatic
467 plumbing system model, which is illustrated in Fig. 13. The melts in equilibrium with
468 both Type-1 Cpx and Type-2 Cpx (Environments A and B) are likely indicative of
469 extensive fractional crystallization resulting in a large range of Ni and Cr contents. In
470 support this interpretation, we note that Amps were formed at the expense of Cpx likely
471 in a peritectic reaction relationship (Fig. 3 and 5), and we speculate that both Type-1
472 Cpx and Type-2 Cpx are “antecrysts” that crystallized from separate mafic to
473 intermediate magma batches. Our geobarometry data indicate that both Type-1 Cpx and
474 Type-2 Cpx formed at depths of 15.3–31.7 km (Tables 3 and DR3); whereas crystal–
475 melt equilibria (Environments C) indicate that the Type-3 Cpx cores are also likely
476 antecrysts characterized by a more primitive rim overgrowth that was in disequilibrium
477 with the host magmas. High Cr and Ni concentrations and X_{Mg} in the Type-3 Cpx rims
478 indicate the overgrowth is the result of mafic magma replenishment (Fig. 5f and Fig.
479 7). The estimated depths where Type-3 Cpx crystallized vary from 14.2 km to 23.0 km
480 (Table 3). The relic Opx with a resorbed boundary is also defined by high Ni and Cr

481 contents, and also indicative of an antecryst origin (Environments D). The overgrowth
482 of relic Opx by Apm implies Opx entered a hydrous magma reservoir.

483 The estimated crystallization depths, at which Amps crystallized, vary from 7.6 km
484 to 13.4 km (Table 3). There is no statistical overlap in terms of crystallization depths
485 between Amps and pyroxenes, indicating that they may have crystallized at different
486 magma reservoirs in the crust, and pyroxenes were overgrown by Amps in a magma
487 reservoir at shallow crustal levels. The lobate boundary between Amp and Pl (Fig. 3e),
488 and the corroded grains of Amp (Fig. 3g) indicate that there is a reactive relationship
489 between Amp and Pl. In addition, some Amps display poikilitic textures with Bts (Fig.
490 3c), indicating that they crystallized from different melts. Considering the low Sr/Y
491 values and relatively high Ce/Pb values of the melts in equilibrium with both large and
492 small Amps, it is likely that these Amps crystallized from other magma reservoirs that
493 are compositionally different from the environments that crystallized the Type-2 Pl,
494 Kfs, and Bt. Therefore, we tend to consider Amps as antecrysts.

495 The sieve-textured Pl core (Type-1 Pl) is likely an antecryst due to its resorbed and
496 most calcic nature, and its equilibrium melt (Environments F) has lower Sr/Rb and
497 Sr/Ba values and higher Ce/Pb values in comparison with melt in equilibrium with the
498 Type-1 Pl rim.

499 We speculate that Environments G, and H that crystallized Type-2 Pl, Bt, Kfs and
500 Qtz are similar due to similar Eu/Eu*, Sr/Y and Ce/Pb values (Figs. 11–12; Tables 1–
501 2). Furthermore, their petrography exhibits the characteristics of paragenetic mineral

502 assemblages (Fig. 3). Thus, these four (Type-2 Pl, Bt, Kfs and Qtz) are reasonably
503 interpreted as orthocrysts which crystallized during the late stage of magma evolution,
504 which is also consistent with the petrographic observations (Fig. 3, Table 1).

505 Melts in equilibrium with pyroxenes collectively display low Sr/Y values, and it is
506 unlikely that these melts developed adakitic signatures through crystal fractionation.
507 Although hornblende fractionation may drive magmas toward high Sr/Y values
508 (Castillo et al., 1999), in this case, we would expect that the melts in equilibrium with
509 the Amps would also gradually evolve towards higher Sr/Y values. Contrary to
510 prediction, all melts in equilibrium with large (Type-1) and small (Type-2) Amps
511 collectively have low Sr/Y values (4.13 to 21.6). From a whole-rock perspective, a
512 negative correlation between $(Dy/Yb)_N$ and $(La/Yb)_N$ is expected for Amp-dominant
513 fractional crystallization (Davidson et al., 2007; He et al., 2011). However, the two
514 ratios show a slight positive correlation for the Zhuyuan granodiorites (grey dashed line
515 with arrowhead in Fig. DR2a).

516 In summary, we identify several different magma batches (environments). Three
517 types of Cpxs and Opx are antecrysts from mafic melts with low Sr/Y but high Ce/Pb
518 values. The different groups of Amp testify to the presence of more than two different
519 melts with low Sr/Y and medium Ce/Pb values. It is difficult to determine whether these
520 Amps have genetic connections with the pyroxenes through fractional crystallization.
521 Meanwhile, the antecrystic Type-1 Pl cores likely crystallized in melt with a more calcic
522 composition than Type-2 Pl. Finally, the late-stage orthocrysts including the Type-2 Pl,

523 Bt, Kfs, and Qtz were probably derived from an intermediate to felsic source with high
524 Sr/Y properties.

525

526 **High Sr/Y melts produced by anatexis of intermediate–felsic rocks under water-**
527 **fluxed condition**

528 Experimental studies show that the fluid-absent breakdown of micas from the
529 intermediate–felsic protoliths may produce melts with low Sr/Rb and Sr/Ba, and
530 notable negative Eu anomalies (Harris et al., 1993; Weinberg and Hasalová, 2015; Zhou
531 et al., 2020). This is consistent with the presence of Kfs as a coexisting peritectic phase
532 in melts generated by muscovite and/or biotite dehydration melting (Harris et al., 1993).
533 In comparison, water-fluxed melting of intermediate–felsic rocks (e.g., diorite,
534 granodiorite, etc.) at mid-crustal levels (0.6–1.2 GPa) will generate felsic magmas with
535 high Sr/Y (Reichardt and Weinberg, 2012; Zhan et al., 2020). Water-fluxed melting
536 (Amp + Pl + Qtz + vapour = melt), where preferential feldspar consumption over micas
537 may leave an Amp-rich residue in the source, leads to felsic melts expected to have
538 positive Eu anomalies, low Rb contents, and high Sr/Rb and Sr/Ba values (Harris et al.,
539 1993; Reichardt and Weinberg, 2012). Simultaneously, these felsic melts may display
540 high Al₂O₃ (> 16 wt.%), low Fe₂O₃^T (< 4.5 wt.%) and elevated Sr concentrations, while
541 exhibiting HREE depletions (Beard and Lofgren 1991; Frost et al. 2016; Zhang et al.,
542 2021).

543 We hypothesize that the resorbed, sieve-textured Pl (Type-1 Pl) core with a relatively
544 high Rb content (10.4–318 ppm) indicates an antecrystic origin (Table 1). By contrast,
545 the high Sr/Y melts in equilibrium with the Type-2 Pl display low Rb contents, high
546 Sr/Rb and Sr/Ba values, and positive Eu anomalies, suggesting that the high Sr/Y melts
547 in equilibrium with them likely formed due to partial melting of intermediate to felsic
548 rocks under water-fluxed conditions. This inference is consistent with the finding that
549 Type-2 Pl crystallized under water-rich conditions (see Section ‘Crystallization
550 Conditions’). Therefore, the high-water contents of the melts in equilibrium with the
551 Type-2 Pl most likely resulted from the anatexis of intermediate–felsic rocks under
552 water-fluxed conditions.

553 Although the whole-rock composition is a mixture of multiple batches of magmas,
554 the late-stage mineral assemblage still dominates the whole-rock compositions because
555 the volume percentage of the rim of Type-1 Pl, Type-2 Pl + Bt + Kfs + Qtz is greater
556 than 75%. Therefore, the whole-rock compositions reflect the first-order characteristics
557 of late-stage melting despite the presence of antecrysts which functions to dilute the
558 high-Sr/Y bulk rock composition. In addition, whole-rock compositions display high
559 Al₂O₃ (15.64–17.32 wt.%) and low Fe₂O₃^T (3.71–5.28 wt.%), and show pronounced
560 HREE depletions ((La/Yb)_N = 15–21). Meanwhile, we note that the addition of
561 antecrystic mafic minerals resulted in higher concentrations of Fe₂O₃^T and decreased
562 Al₂O₃ in whole-rock compositions. Accordingly, the late-stage felsic melt typically has
563 higher Al₂O₃, but lower Fe₂O₃^T contents. However, melts produced by water-flux

564 melting of intermediate to felsic rocks under 0.6–1.2 GPa are generally characterized
565 by high Al₂O₃ (> 16 wt.%) and low Fe₂O₃^T (< 4.5 wt.%) (Beard & Lofgren, 1991, Frost
566 et al., 2016), which coincide with late-stage melt compositions of the Zhuyuan
567 granodiorites.

568 Moreover, the low Rb and high Sr contents of the melts in equilibrium with the Type-
569 2 Pl also argues against an extensive fractionation process, thus ruling out the possibility
570 that the high-water content is caused by the high degrees of fractional crystallization
571 (Wang et al., 2017). Accordingly, we conclude that the late-stage orthocryst assemblage
572 represents the near-primary high-Sr/Y composition derived from water-fluxed melting
573 of intermediate to felsic source rocks. Meanwhile, the high Sr/Y signal of felsic melts
574 was diluted by magma recharge, leading to more mafic compositions in the bulk.

575

576 **Modeling for source rock compositions**

577 To further elucidate the dilution of the high Sr/Y properties of late-stage felsic melt
578 by antecrysts with low Sr/Y values, and to identify the possible sources of these late-
579 stage melts, we carried out simple quantitative simulations. We assume sample ZY17-
580 8 (Opx free) to represent a melt composition that is least affected by the low-Sr/Y
581 antecrysts, given that it is one of the samples with the highest SiO₂ contents (67.16
582 wt.%) and relatively low Mg# value (50; Table DR2; Xie et al., 2023). The proportion
583 of various rock-forming minerals in the sample is estimated using mass balance
584 calculations (Li et al., 2020b). The calculated results (Table DR7) are in good

585 agreement with the petrographic observations. We estimate the interstitial magma
586 compositions (i.e., the ‘undiluted melt’) by removing the mass of antecrysts. After
587 deducting the intermediate-mafic antecrysts, the remaining bulk composition shows
588 high SiO₂ content (70.33 wt.%), low Mg# value (31.4), and significantly increased Sr
589 content (555 ppm) and Sr/Y value (132). By comparing the whole-rock Sr/Y value
590 (36.3) of sample ZY17-8, we confirm that the adakitic signals of the high-Sr/Y melts
591 are significantly weakened by the incorporation of intermediate-mafic antecrysts. Thus,
592 antecryst entrainment is crucial for understanding the geochemical diversity of granitic
593 magmas with an adakitic signature, and whole-rock compositions of granitoids
594 probably deviate remarkably the original melt compositions (Werts et al., 2020).

595 To quantitatively simulate the nature of the source rock, we assumed that the high
596 Sr/Y ‘undiluted melt’ calculated based on sample ZY17-8 with the highest Zr/Hf value
597 is the near-primary melt derived from partial melting of intermediate–felsic source rock.
598 When the residual solid phase and melt fraction (i.e., the degree of partial melting) can
599 be reasonably constrained, the trace element compositions of the source rock can be
600 calculated from known melt compositions using the batch melting model of Shaw
601 (1970):

$$602 \quad C_0^i = C_L^i * (D_{\text{Bulk}}^i + F * (1 - D_{\text{Bulk}}^i))$$

603 where C₀ⁱ and C_Lⁱ represent the concentration of element i in the source rock and melt,
604 respectively; F is the melt fraction of source rock; and D_{Bulk}ⁱ is the bulk partition
605 coefficient of element i, which is the sum of the partition coefficient (D) for each

606 mineral multiplied by the weight percentage of corresponding mineral in the residual
607 solid phase ($D_{\text{Bulk}}^i = D_S^i * W_S$).

608 We compared the major elements of the undiluted melt with that of experimental
609 melts derived from the partial melting of a range of crustal protoliths compiled by Gao
610 et al. (2016), Weinberg and Hasalová (2015), and Zhan et al. (2020). To find the best
611 matching experimental melt compositions, the sum of square of the deviations of each
612 major element oxides between experimental melts and undiluted melt was calculated.
613 Based on the discussion above regarding water-fluxed melting, only the melting
614 experiments of intermediate–felsic source rocks under water-presence conditions are
615 considered here. We report the four best matching experimental melts (the sum of
616 squared of the deviations is less than 10), and the corresponding partial melting
617 pressures, melt fractions, and proportion of residual solid phases (Experiments 1–4 in
618 Table DR7).

619 We also explore the trace element composition of the source rocks (e.g., REE, Sr,
620 and Y) of undiluted melt (inferred from sample ZY17-8) using compositionally
621 appropriate mineral partition coefficients (Table DR7) and the batch melting equation.
622 The calculated trace element compositions under different melting conditions
623 corresponding to the four experiments are listed in Table DR7 and are plotted in Fig.
624 14. The modeling results show that different source rocks may have different
625 implications for constraining the derivation of high Sr/Y granites.

626 We find that the calculated trace elements of intermediate-felsic sources

627 corresponding to different melting conditions are characterized by significant positive
628 Eu anomalies (1.66-3.96), indicating that the plagioclase accumulation in the source
629 rocks is particularly important for melting to produce high Sr/Y melt. This is consistent
630 with the interpretations proposed by Shi et al. (2022) and Wang et al. (2022). In addition,
631 we find the following results:

632 (1) In the experimental runs under high pressure conditions (Exp 1, 800°C, 1.5 GPa,
633 5 wt% H₂O; Koester et al., 2002), the partial melting degree of source rocks is relatively
634 low (21%). The calculated source rock shows a low Sr/Y value (21.9), which is mainly
635 due to the fact that the source rock contains a considerable proportion of garnet (Grt)
636 and Amp. Therefore, for Exp 1 to produce the high Sr/Y melt, it is necessary to have a
637 significant amount of residual Y-rich minerals dominated by Grt in the source.

638 (2) In the experimental runs under moderate pressure conditions (Exp 2, 850°C, 1
639 GPa, 2 wt% H₂O; García-Arias et al., 2012), the partial melting degree of source rocks
640 is relatively high (61%), with minor Grt in the residues (< 1 wt%). Our modeling result
641 for source rock exhibits a relatively high Sr/Y value (98.9), which is most likely due to
642 the high abundance of feldspar but low abundance of Grt in the source. Moreover, the
643 high Sr/Y signal of the partial melt is mainly attributed to significant melting of feldspar
644 in the source rocks, releasing large amounts of Sr into the melt.

645 (3) In the moderate-low pressure melting experiment of Grt-bearing metasedimen-
646 tary gneiss (Exp 3, 800°C, 0.7 GPa, 5.1 wt% H₂O; Ward et al., 2008), the degree of
647 partial melting in the source rocks is relatively high (67%). Feldspar is absent in the

648 residues, but some Y-rich minerals (Grt + Amp) are retained. In addition, the calculated
649 source rock shows the least obvious positive Eu anomaly ($\text{Eu}/\text{Eu}^* = 1.66$) and have
650 much lower Sr content (183 ppm) and Sr/Y value (12.6). These results indicate that the
651 high Sr/Y signal of the partial melt requires concurrent feldspar melting and retention
652 of an Y-rich mineral in the residue.

653 (4) In the low-pressure melting experiment of biotite tonalite (Exp 4, 690°C, 0.599
654 GPa, H₂O-saturated; Watkins et al., 2007), the moderate degree of partial melting (32%)
655 produces a melt with major elements comparable to undiluted melt of sample ZY17-8.
656 The calculated trace elements of this biotite tonalite (source rock) is characterized by
657 strongly fractionated REE patterns (Fig. 14), strong positive Eu anomalies and high
658 $(\text{La}/\text{Yb})_{\text{N}}$ (265) and Sr/Y (191) values. Furthermore, Y-rich minerals are absent in the
659 residues of Exp 4, and some feldspar is present. Therefore, the high Sr/Y signal of the
660 partial melt corresponding to Exp 4 is completely inherited from the source rock, mainly
661 through the melting of large amounts of feldspar under water-saturated condition.

662 In summary, for intermediate-felsic sources, water-present to water-saturated partial
663 melting at high to low pressures (corresponding to 0.599 GPa to 1.5 GPa) may produce
664 the high Sr/Y and $(\text{La}/\text{Yb})_{\text{N}}$ signatures of the Zhuyuan granodiorites. We also note that
665 high Sr/Y and $(\text{La}/\text{Yb})_{\text{N}}$ values are produced even when the source rock contains no or
666 very little Y-rich minerals (Grt + Amp). However, when Y-rich minerals are enriched in
667 source rocks, high-Sr/Y melts may also be produced by melting a large amount of feld-
668 spar while retaining considerable amounts of Y-rich minerals in the sources. Thus, we

669 suggest that the Zhuyuan high-Sr/Y melts were produced under various pressure con-
670 ditions, and not limited to high pressures (> 1.5 GPa). Previous studies have also con-
671 firmed that felsic melt with adakitic signatures can be generated at much lower pres-
672 sures (0.6–1.2 GPa, e.g., Zhan et al., 2020). Accordingly, high Sr/Y adakitic granites
673 cannot be directly used to infer the thickness of the continental crust when the source
674 is a felsic to intermediate protolith melted under water-fluxed conditions.

675

676

IMPLICATIONS

677 Our study highlights that the adakitic signatures in plutonic rocks are not only
678 significantly influenced by the stability (e.g., high pressure conditions) and modal
679 abundance of source residual minerals (Moyen, 2009), but also by the variations in
680 source lithology and water content (Johnson et al., 2017; Ma et al., 2015; Pourteau et
681 al., 2020). For example, magmas with adakitic affinity can be generated by water-fluxed
682 melting of intermediate to felsic rocks under various pressures (Moyen, 2009). In
683 addition, antecryst recycling processes in granitic magma systems are common (Barnes
684 et al., 2019; Oppenheim et al. 2021). Injection by diverse magma batches with various
685 types of non-orthocrysts could significantly obscure the evolutionary path of the
686 primary magmas. Our study clearly reveals that the high Sr/Y signal of primary adakitic
687 melts can be diluted by the addition of non-orthocrysts or other batches of melts with
688 low Sr/Y values. From this perspective, estimates of paleo-crustal thickness based on
689 whole-rock granitic compositions (Profeta et al., 2015; Hu et al., 2017) should be

690 considered with caution due to the possibility of open-system behavior that may have
691 affected original melt compositions.

692

693 **ACKNOWLEDGEMENTS AND FUNDING**

694 We would like to express our sincere gratitude to Editor Rachel Russell and
695 Associate Editor Callum Hetherington for their efficient handling of our manuscript
696 and valuable insights. We would also like to thank Reviewers Kenneth Johnson and
697 John Adam for their constructive comments, which have greatly contributed to the
698 improvement of our paper. Additionally, we thank Yuan-Yuan Xiao and Qiong-Yao
699 Zhan for assistance with many helpful discussions. This work was jointly funded by the
700 State Key Program of National Natural Science of China (Grant No. 41730426), the
701 National Natural Science Foundation of China (Grant Nos. 41872066, 41872082 and
702 41702069), the Fundamental Research Funds for the Central Universities of China
703 (2652018121), and the Open Research Funds for GPMR (Grant GPMR201509).

704

705 **REFERENCES CITED**

706 Bach, P., Smith, I.E.M. and Malpas, J.G. (2012) The Origin of Garnets in Andesitic
707 Rocks from the Northland Arc, New Zealand, and their Implication for Sub-arc
708 Processes. *Journal of Petrology*, 53, 1169–1195.

709 Barnes, C.G., Werts, K., Memeti, V. and Ardill, K. (2019) Most Granitoid Rocks are
710 Cumulates: Deductions from Hornblende Compositions and Zircon Saturation.

- 711 Journal of Petrology, 60, 2227–2240.
- 712 Beard, J.S. and Lofgren, G.E. (1991) Dehydration melting and water-saturated melting
713 of basaltic and andesitic greenstones and amphibolites at 1, 3, and 6.9 kb. Journal
714 of Petrology, 32, 365–401.
- 715 Bédard, J.H. (2001) Parental magmas of the Nain Plutonic Suite anorthosites and mafic
716 cumulates: a trace element modelling approach. Contributions to Mineralogy and
717 Petrology, 141, 747–771.
- 718 Bindeman, I.N., Davis, A.M. and Drake, M.J. (1998) Ion microprobe study of
719 plagioclase-basalt partition experiments at natural concentration levels of trace
720 elements. Geochimica et Cosmochimica Acta, 62, 1175–1193.
- 721 Bloch, E.M., Jollands, M.C., Tollan, P., Plane, F., Bouvier, A.S., Hervig, R., Berry, A.J.,
722 Zaubitzer, C., Escrig, S., Müntener, O., Ibañez-Mejia, M., Alleon, J., Meibom, A.,
723 Baumgartner, L.P., Marin-Carbonne, J. and Newville, M. (2022) Diffusion
724 anisotropy of Ti in zircon and implications for Ti-in-zircon thermometry. Earth and
725 Planetary Science Letters, 578, 117317.
- 726 Blundy, J. and Cashman, K. (2008) Petrologic Reconstruction of Magmatic System
727 Variables and Processes. Reviews in Mineralogy and Geochemistry, 69, 179–239.
- 728 Brackman, A.J. and Schwartz, J.J. (2022) The formation of high-Sr/Y plutons in
729 cordilleran-arc crust by crystal accumulation and melt loss. Geosphere, 18, 370–
730 393.
- 731 Burney, D., Peate, D.W., Riishuus, M.S. and Ukstins, I.A. (2020) Reconstructing the

- 732 plumbing system of an off-rift primitive alkaline tuya (Vatnafell, Iceland) using
733 geothermobarometry and CSDs. *Journal of Volcanology and Geothermal*
734 *Research*, 399, 106914.
- 735 Calmus, T., Aguillon-Robles, A., Maury, R.C., Bellon, H., Benoit, M., Cotten, J.,
736 Bourgois, J. and Michaud, F. (2003) Spatial and temporal evolution of basalts and
737 magnesian andesites (bajaites) from Baja California, Mexico: the role of slab
738 melts. *Lithos*, 66, 77–105.
- 739 Cashman, K.V., Sparks, R.S. and Blundy, J.D. (2017) Vertically extensive and unstable
740 magmatic systems: A unified view of igneous processes. *Science*, 355, eaag3055.
- 741 Castillo, P.R. (2012) Adakite petrogenesis. *Lithos*, 134, 304–316.
- 742 Castillo, P.R., Janney, P.E. and Solidum, R.U. (1999) Petrology and geochemistry of
743 Camiguin Island, southern Philippines: insights to the source of adakites and other
744 lavas in a complex arc setting. *Contributions to Mineralogy and Petrology*, 134,
745 33–51.
- 746 Chen, S., Niu, Y., Li, J., Sun, W., Zhang, Y., Hu, Y. and Shao, F. (2016) Syn-collisional
747 adakitic granodiorites formed by fractional crystallization: Insights from their
748 enclosed mafic magmatic enclaves (MMEs) in the Qumushan pluton, North Qilian
749 Orogen at the northern margin of the Tibetan Plateau. *Lithos*, 248, 455–468.
- 750 Clemens, J.D. and Stevens, G. (2012) What controls chemical variation in granitic
751 magmas? *Lithos*, 134, 317–329.
- 752 Collins, W.J., Murphy, J.B., Johnson, T.E. and Huang, H. (2020) Critical role of water

- 753 in the formation of continental crust. *Nature Geoscience*, 13, 331–338.
- 754 Davidson, J., Turner, S., Handley, H., Macpherson, C. and Dosseto, A. (2007)
- 755 Amphibole “sponge” in arc crust? *Geology*, 35, 787–790.
- 756 Defant, M.J. and Drummond, M.S. (1990) Derivation of some modern arc magmas by
- 757 melting of young subducted lithosphere. *Nature*, 347, 662–665.
- 758 Elkins, L.J., Gaetani, G.A. and Sims, K.W.W. (2008) Partitioning of U and Th during
- 759 garnet pyroxenite partial melting: Constraints on the source of alkaline ocean
- 760 island basalts. *Earth and Planetary Science Letters*, 265, 270–286.
- 761 Ewart, A. and Griffin, W.L. (1994) Application of Proton-Microprobe Data to Trace-
- 762 Element Partitioning in Volcanic-Rocks. *Chemical Geology*, 117, 251–224.
- 763 Foster, M.D. (1960) Interpretation of the Composition of Trioctahedral Micas, United
- 764 States Geological Survey Professional Paper, 354, 1–49.
- 765 Frost, C.D., Swapp, S.M., Frost, B.R., Finley-Blasi, L. and Fitz-Gerald, D.B. (2016)
- 766 Leucogranites of the Teton Range, Wyoming: A record of Archean collisional
- 767 orogeny. *Geochimica et Cosmochimica Acta*, 185, 528–549.
- 768 Fu, B., Page, F.Z., Cavosie, A.J., Fournelle, J., Kita, N.T., Lackey, J.S., Wilde, S.A. and
- 769 Valley, J.W. (2008) Ti-in-zircon thermometry: applications and limitations.
- 770 *Contributions to Mineralogy and Petrology*, 156, 197–215.
- 771 Gao, P., Zheng, Y.F. and Zhao, Z.F. (2016) Experimental melts from crustal rocks: A
- 772 lithochemical constraint on granite petrogenesis. *Lithos*, 266-267, 133–157.
- 773 García-Arias, M., Corretgé, L.G. and Castro, A. (2012) Trace element behavior during

- 774 partial melting of Iberian orthogneisses: An experimental study. *Chemical*
775 *Geology*, 292, 1–17.
- 776 Graham, B., Dunning, G. and Leitch, A. (2020) Magma Mushes of the Fogo Island
777 Batholith: a Study of Magmatic Processes at Multiple Scales. *Journal of Petrology*,
778 61, ega097.
- 779 Guo, F., Nakamura, E., Fan, W., Kobayoshi, K. and Li, C. (2007) Generation of
780 Palaeocene Adakitic Andesites by Magma Mixing; Yanji Area, NE China. *Journal*
781 *of Petrology*, 48, 661–692.
- 782 Harris, N., Massey, J. and Iner, S. (1993) The role of fluids in the formation of High
783 Himalayan leucogranites. Geological Society, London, Special Publications, 74,
784 391.
- 785 He, Y., Li, S., Hoefs, J., Huang, F., Liu, S.-A. and Hou, Z. (2011) Post-collisional
786 granitoids from the Dabie orogen: New evidence for partial melting of a thickened
787 continental crust. *Geochimica et Cosmochimica Acta*, 75, 3815–3838.
- 788 Higgins, M.D. (1996) Crystal size distributions and other quantitative textural
789 measurements in lavas and tuff from Egmont volcano (Mt. Taranaki), New
790 Zealand. *Bulletin of Volcanology*, 58, 194–204.
- 791 Higgins, O., Sheldrake, T. and Caricchi, L. (2022) Machine learning thermobarometry
792 and chemometry using amphibole and clinopyroxene: a window into the roots of
793 an arc volcano (Mount Liamuiga, Saint Kitts). *Contributions to Mineralogy and*
794 *Petrology*, 177, 1–22.

- 795 Hofmann, A.W., Jochum, K.P., Seufert, M. and White, W.M. (1986) Nb and Pb in
796 oceanic basalts: new constraints on mantle evolution. *Earth and Planetary Science*
797 *Letters*, 33–45.
- 798 Holland, T. and Blundy, J. (1994) Non-ideal interactions in calcic amphiboles and their
799 bearing on amphibole–plagioclase thermometry. *Contributions to Mineralogy and*
800 *Petrology*, 116, 433–447.
- 801 Hollings, P., Sievwright, R.H., Buret, Y., Wilkinson, J.J., Loader, M.A. and Nathwani,
802 C.L. (2020) Multi-stage arc magma evolution recorded by apatite in volcanic
803 rocks. *Geology*, 48, 323–327.
- 804 Hu, F., Ducea, M.N., Liu, S. and Chapman, J.B. (2017) Quantifying Crustal Thickness
805 in Continental Collisional Belts: Global Perspective and a Geologic Application.
806 *Scientific Reports*, 7, 7058.
- 807 Hu, J., Li, X., Xu, J., Mo, X., Wang, F., Yu, H., Shan, W., Xing, H., Huang, X. and
808 Dong, G. (2019) Generation of coeval metaluminous and muscovite-bearing
809 peraluminous granitoids in the same composite pluton in West Qinling, NE Tibetan
810 Plateau. *Lithos*, 344, 374–392.
- 811 Humphreys, M.C.S., Cooper, G.F., Zhang, J., Loewen, M., Kent, A.J.R., Macpherson,
812 C.G. and Davidson, J.P. (2019) Unravelling the complexity of magma plumbing
813 at Mount St. Helens: a new trace element partitioning scheme for amphibole.
814 *Contributions to Mineralogy and Petrology*, 174, 1–15.
- 815 Jerram, D.A., Dobson, K.J., Morgan, D.J. and Pankhurst, M.J. (2018) The Petrogenesis

- 816 of Magmatic Systems: Using Igneous Textures to Understand Magmatic
817 Processes, Volcanic and Igneous Plumbing Systems, Elsevier, 191–229.
- 818 Jerram, D.A. and Martin, V.M. (2008) Understanding crystal populations and their
819 significance through the magma plumbing system. Geological Society, London,
820 Special Publications, 304, 133–148.
- 821 Ji, Z., Ge, W., Yang, H., Tian, D., Chen, H. and Zhang, Y. (2018) Late Carboniferous–
822 Early Permian high- and low-Sr/Y granitoids of the Xing'an Block, northeastern
823 China: Implications for the late Paleozoic tectonic evolution of the eastern Central
824 Asian Orogenic Belt. *Lithos*, 322, 179–196.
- 825 Johnson, T.E., Brown, M., Gardiner, N.J., Kirkland, C.L. and Smithies, R.H. (2017)
826 Earth's first stable continents did not form by subduction. *Nature*, 543, 239–242.
- 827 Kay, R. and Kay, S. (1993) Delamination and magmatism. *Tectonophysics*, 219, 177–
828 189.
- 829 Kay, R.W. (1978) Aleutian magnesian andesites: Melts from subducted Pacific ocean
830 crust. *Journal of Volcanology and Geothermal Research*, 4, 117–132.
- 831 Koester, E., Pawley, A.R., Fernandes, L.A.D., Porcher, C.C. and Soliani, J.R.E. (2002)
832 Experimental melting of cordierite gneiss and the petrogenesis of syntranscurrent
833 peraluminous granites in southern Brazil. *Journal of Petrology*, 1595–1616.
- 834 Lange, R.A., Frey, H.M. and Hector, J. (2009) A thermodynamic model for the
835 plagioclase–liquid hygrometer/thermometer. *American Mineralogist*, 94, 494–
836 506.

- 837 Leake, B.E., Woolley, A.R. and Birch, W.D. (1997) Nomenclature of Amphiboles:
838 Report of the Subcommittee on Amphiboles of the International Mineralogical
839 Association Commission on New Minerals and Mineral Names. Mineralogical
840 Magazine, 61, 295–321.
- 841 Li, X., Mo, X., Huang, X., Dong, G., Yu, X., Luo, M. and Liu, Y. (2015) U–Pb zircon
842 geochronology, geochemical and Sr–Nd–Hf isotopic compositions of the Early
843 Indosinian Tongren Pluton in West Qinling: Petrogenesis and geodynamic
844 implications. *Journal of Asian Earth Sciences*, 97, 38–50.
- 845 Li, X., Zhang, C., Almeev, R.R. and Holtz, F. (2020a) GeoBalance: An Excel VBA
846 program for mass balance calculation in geosciences. *Geochemistry*, 80, 125629.
- 847 Li, X., Zhang, C., Behrens, H. and Holtz, F. (2020b) Calculating amphibole formula
848 from electron microprobe analysis data using a machine learning method based on
849 principal components regression. *Lithos*, 362–363.
- 850 Lu, Y. (2005) GeoKit-A geochemical toolkit for Microsoft Excel. *Geochimica*, 35, 459–
851 464 (in Chinese with English abstract).
- 852 Luo, B., Zhang, H. and Lü, X. (2012) U–Pb zircon dating, geochemical and Sr–Nd–Hf
853 isotopic compositions of Early Indosinian intrusive rocks in West Qinling, central
854 China: petrogenesis and tectonic implications. *Contributions to Mineralogy and
855 Petrology*, 164, 551–569.
- 856 Ma, Q., Zheng, J.P., Xu, Y.G., Griffin, W.L. and Zhang, R.S. (2015) Are continental
857 “adakites” derived from thickened or foundered lower crust? *Earth and Planetary*

- 858 Science Letters, 419, 125–133.
- 859 Macpherson, C.G., Dreher, S.T. and Thirlwall, M.F. (2006) Adakites without slab
860 melting: High pressure differentiation of island arc magma, Mindanao, the
861 Philippines. *Earth and Planetary Science Letters*, 243, 581–593.
- 862 Marsh, B.D. (1988) Crystal size distribution (CSD) in rocks and the kinetics and
863 dynamics of crystallization. *Contributions to Mineralogy Petrology*, 99, 277–291.
- 864 Martin, H., Smithies, R.H., Rapp, R., Moyen, J.F. and Champion, D. (2005) An
865 overview of adakite, tonalite–trondhjemite–granodiorite (TTG), and sanukitoid:
866 relationships and some implications for crustal evolution. *Lithos*, 79, 1–24.
- 867 Miller, J.S., Matzel, J.E.P., Miller, C.F., Burgess, S.D. and Miller, R.B. (2007) Zircon
868 growth and recycling during the assembly of large, composite arc plutons. *Journal*
869 *of Volcanology and Geothermal Research*, 167, 282–299.
- 870 Morgan, D.J., Jerram, D.A., Chertkoff, D.G., Davidson, J.P., Pearson, D.G., Kronz, A.
871 and Nowell, G.M. (2007) Combining CSD and isotopic microanalysis: Magma
872 supply and mixing processes at Stromboli Volcano, Aeolian Islands, Italy. *Earth*
873 *and Planetary Science Letters*, 260, 419–431.
- 874 Morimoto, N., Fabries, J., Ferguson, A.K., Ginzburg, I.V., Ross, M., Seifert, F.A.,
875 Zussman, J., Aoki, K. and Gottardi, G. (1988) Nomenclature of Pyroxenes.
876 *Mineralogical Magazine*, 52, 535–550.
- 877 Moyen, J.-F. (2009) High Sr/Y and La/Yb ratios: The meaning of the “adakitic
878 signature”. *Lithos*, 112, 556–574.

- 879 Nachit, H., Ibhi, A., Abia, E.H. and Ben Ohoud, M. (2005) Discrimination between
880 primary magmatic biotites, reequilibrated biotites and neoformed biotites.
881 *Comptes Rendus Geoscience*, 337, 1415–1420.
- 882 Namur, O., Montalbano, S., Bolle, O. and Vander Auwera, J. (2020) Petrology of the
883 April 2015 Eruption of Calbuco Volcano, Southern Chile. *Journal of Petrology*, 61,
884 ega084.
- 885 Nandedkar, R. H., Hürlimann, N., Ulmer, P. & Müntener, O. (2016) Amphibole-melt
886 trace element partitioning of fractionating calc-alkaline magmas in the lower crust:
887 an experimental study. *Contributions to Mineralogy and Petrology*, 171, 1–25.
- 888 Nash, P.W. (1985) Partition coefficients for trace elements in silicic magmas.
889 *Geochimica et Cosmochimica Acta*, 49, 2309–2322.
- 890 Neave, D.A., Bali, E., Guðfinnsson, G.H., Halldórsson, S.A., Kahl, M., Schmidt, A.-S.
891 and Holtz, F. (2019) Clinopyroxene–Liquid Equilibria and Geothermobarometry
892 in Natural and Experimental Tholeiites: the 2014–2015 Holuhraun Eruption,
893 Iceland. *Journal of Petrology*, 60, 1653–1680.
- 894 Neave, D.A. and Putirka, K.D. (2017) A new clinopyroxene-liquid barometer, and
895 implications for magma storage pressures under Icelandic rift zones. *American*
896 *Mineralogist*, 102, 777–794.
- 897 Oppenheim, L. F., Memeti, V., Barnes, C. G., Chambers, M., Krause, J., & Esposito, R.
898 (2021) Feldspar recycling across magma mush bodies during the voluminous Half
899 Dome and Cathedral Peak stages of the Tuolumne intrusive complex, Yosemite

- 900 National Park, California, USA. *Geosphere*, 17(2), 322-351.
- 901 Ou, Q., Wang, Q., Wyman, D.A., Zhang, H., Yang, J., Zeng, J., Hao, L., Chen, Y., Liang,
902 H. and Qi, Y. (2017) Eocene adakitic porphyries in the central-northern Qiangtang
903 Block, central Tibet: Partial melting of thickened lower crust and implications for
904 initial surface uplifting of the plateau. *Journal of Geophysical Research: Solid
905 Earth*, 122, 1025–1053.
- 906 Paterson, S., Memeti, V., Mundil, R. and Žák, J. (2016) Repeated, multiscale, magmatic
907 erosion and recycling in an upper-crustal pluton: Implications for magma chamber
908 dynamics and magma volume estimates. *American Mineralogist*, 101, 2176–2198.
- 909 Patiño Douce, A.E. (1999) What do experiments tell us about the relative contributions
910 of crust and mantle to the origin of granitic magmas? Geological Society, London,
911 Special Publications, 168, 55–75.
- 912 Pichavant, M. and Macdonald, R. (2007) Crystallization of primitive basaltic magmas
913 at crustal pressures and genesis of the calc-alkaline igneous suite: experimental
914 evidence from St Vincent, Lesser Antilles arc. *Contributions to Mineralogy and
915 Petrology*, 154, 535–558.
- 916 Pourteau, A., Doucet, L.S., Blereau, E.R., Volante, S., Johnson, T.E., Collins, W.J., Li,
917 Z.-X. and Champion, D.C. (2020) TTG generation by fluid-fluxed crustal melting:
918 Direct evidence from the Proterozoic Georgetown Inlier, NE Australia. *Earth and
919 Planetary Science Letters*, 550, 116548.
- 920 Price, R.C., Gamble, J.A., Smith, I.E.M., Maas, R., Waight, T., Stewart, R.B. and

- 921 Woodhead, J. (2012) The Anatomy of an Andesite Volcano: a Time–Stratigraphic
922 Study of Andesite Petrogenesis and Crustal Evolution at Ruapehu Volcano, New
923 Zealand. *Journal of Petrology*, 53, 2139–2189.
- 924 Profeta, L., Ducea, M.N., Chapman, J.B., Paterson, S.R., Gonzales, S.M., Kirsch, M.,
925 Petrescu, L. and DeCelles, P.G. (2015) Quantifying crustal thickness over time in
926 magmatic arcs. *Scientific Reports*, 5, 17786.
- 927 Putirka, K. (2016) Amphibole thermometers and barometers for igneous systems and
928 some implications for eruption mechanisms of felsic magmas at arc volcanoes.
929 *American Mineralogist*, 101, 841–858.
- 930 Putirka, K.D. (2008) Thermometers and Barometers for Volcanic Systems. *Reviews in*
931 *Mineralogy and Geochemistry*, 69, 61–120.
- 932 Reichardt, H. and Weinberg, R.F. (2012) Hornblende Chemistry in Meta- and Diatexites
933 and its Retention in the Source of Leucogranites: an Example from the Karakoram
934 Shear Zone, NW India. *Journal of Petrology*, 53, 1287–1318.
- 935 Schiller, D. and Finger, F. (2019) Application of Ti-in-zircon thermometry to granite
936 studies: problems and possible solutions. *Contributions to Mineralogy and*
937 *Petrology*, 174, 1–16.
- 938 Schnetzler, C.C. and Philpotts, J.A. (1970) Partition coefficients of rare-earth elements
939 between igneous matrix material and rock-forming mineral phenocrysts; II.
940 *Geochimica et Cosmochimica Acta*, 34, 331–340.
- 941 Shaw, D.M. (1970) Trace element fractionation during anatexis. *Geochimica et*

- 942 Cosmochimica Acta, 34, 237–243.
- 943 Shen, Y., Zheng, Y.-C., Hou, Z.-Q., Zhang, A.-P., Huizenga, J.M., Wang, Z.-X. and
944 Wang, L. (2021) Petrology of the Machangqing Complex in Southeastern Tibet:
945 Implications for the Genesis of Potassium-rich Adakite-like Intrusions in
946 Collisional Zones. *Journal of Petrology*, 62, egab066.
- 947 Shi, H., Xia, Y., Xu, X., Zhu, J. and He, J. (2022) Crystal-melt separation of the
948 Cretaceous volcanic-plutonic complex in SE China: High Sr/Y rocks generated by
949 plagioclase accumulation. *Lithos*, 106848.
- 950 Shimizu, K., Liang, Y., Sun, C., Jackson, C.R.M. and Saal, A.E. (2017) Parameterized
951 lattice strain models for REE partitioning between amphibole and silicate melt.
952 *American Mineralogist*, 102, 2254–2267.
- 953 Sims, K.W.W. and DePaolo, D.J. (1997) Inferences about mantle magma sources from
954 incompatible element concentration ratios in oceanic basalts. *Geochimica et*
955 *Cosmochimica Acta*, 61, 765–784.
- 956 Sisson, T.W. and Grove, T.L. (1993) Experimental investigations of the role of H₂O in
957 calc-alkaline differentiation and subduction zone magmatism. *Contributions to*
958 *Mineralogy and Petrology*, 113, 143–166.
- 959 Smith, J.V. (1974) *Feldspar Minerals. Volume 1. Crystal Structure and Physical*
960 *Properties*. Berlin: Springer, 625.
- 961 Stern, C.R. and Kilian, R. (1996) Role of the subducted slab, mantle wedge and
962 continental crust in the generation of adakites from the Andean Austral Volcanic

- 963 Zone. *Contributions to Mineralogy and Petrology*, 123, 263–281.
- 964 Streckeisen, A.L. (1976) Classification of the common igneous rocks by means of their
965 chemical composition: A provisional attempt. *Neues Jahrbuch für Mineralogie,*
966 *Monatshefte*, 1, 1–15.
- 967 Sun, C., Graff, M. and Liang, Y. (2017) Trace element partitioning between plagioclase
968 and silicate melt: The importance of temperature and plagioclase composition,
969 with implications for terrestrial and lunar magmatism. *Geochimica et*
970 *Cosmochimica Acta*, 206, 273–295.
- 971 Sun, S.S. and McDonough, W.F. (1989) Chemical and isotopic systematics of oceanic
972 basalts: implications for mantle composition and processes. Geological Society,
973 London, Special Publications, 42, 313–345.
- 974 Wang, D., Liu, J., Carranza, E.J.M., Zhai, D., Wang, Y., Zhen, S., Wang, J., Wang, J.,
975 Liu, Z. and Zhang, F. (2019) Formation and evolution of snowball quartz
976 phenocrysts in the Dongping porphyritic granite, Hebei Province, China: Insights
977 from fluid inclusions, cathodoluminescence, trace elements, and crystal size
978 distribution study. *Lithos*, 340, 239–254.
- 979 Wang, L.J., Guo, J.H., Yin, C. and Peng, P. (2017) Petrogenesis of ca. 1.95 Ga meta-
980 leucogranites from the Jining Complex in the Khondalite Belt, North China
981 Craton: Water-fluxed melting of metasedimentary rocks. *Precambrian Research*,
982 303, 355–371.
- 983 Wang, P., Zhao, G., Liu, Q., Yao, J., Han, Y. and Li, J. (2022) Effect of source

- 984 compositions on adakitic features: A case study from the Buya granite, in western
985 Kunlun, NW China. *American Journal of Science*, 322, 828–850.
- 986 Ward, R., Stevens, G. and Kisters, A. (2008) Fluid and deformation induced partial
987 melting and melt volumes in low-temperature granulite-facies metasediments,
988 Damara Belt, Namibia. *Lithos*, 105, 253–271.
- 989 Waters, L.E. and Lange, R.A. (2015) An updated calibration of the plagioclase-liquid
990 hygrometer-thermometer applicable to basalts through rhyolites. *American*
991 *Mineralogist*, 100, 2172–2184.
- 992 Watkins, J.M., Clemens, J.D. and Treloar, P.J. (2007) Archaean TTGs as sources of
993 younger granitic magmas: melting of sodic metatonalites at 0.6–1.2 GPa.
994 *Contributions to Mineralogy and Petrology*, 154, 91–110.
- 995 Watson, E.B., Wark, D.A. and Thomas, J.B. (2006) Crystallization thermometers for
996 zircon and rutile. *Contributions to Mineralogy and Petrology*, 151, 413–433.
- 997 Weinberg, R.F. and Hasalová, P. (2015) Water-fluxed melting of the continental crust:
998 A review. *Lithos*, 212, 158–188.
- 999 Werts, K., Barnes, C.G., Memeti, V., Ratschbacher, B., Williams, D. and Paterson, S.R.
1000 (2020) Hornblende as a tool for assessing mineral–melt equilibrium and
1001 recognition of crystal accumulation. *American Mineralogist*, 105, 77–91.
- 1002 Wieser, P.E., Jenner, F., Edmonds, M., Maclennan, J. and Kunz, B.E. (2020)
1003 Chalcophile elements track the fate of sulfur at Kīlauea Volcano, Hawai’i.
1004 *Geochimica et Cosmochimica Acta*, 282, 245–275.

- 1005 Xie, Y. H., Li, X. W., Mo, X. X., Dong, G. C., Sun, Y. Q. & Shan, W. (2023) The effects
1006 of the source composition on the origin of orthopyroxene-bearing adakitic
1007 granitoid in West Qinling, Central China. *Geoscience Frontiers*, 14(3), 101554.
- 1008 Xing, H., Li, X., Xu, J., Mo, X., Shan, W., Yu, H., Hu, J., Huang, X. and Dong, G.
1009 (2020) The genesis of felsic magmatism during the closure of the Northeastern
1010 Paleo-Tethys Ocean: Evidence from the Heri batholith in West Qinling, China.
1011 *Gondwana Research*, 84, 38–51.
- 1012 Xu, X., Dong, C., Li, W. and Zhou, X. (1999) Late Mesozoic intrusive complexes in
1013 the coastal area of Fujian, SE China: the significance of the gabbro-diorite–granite
1014 association. *Lithos*, 46, 299–315.
- 1015 Yang, Z.F., Luo, Z.H. and Lu, X.X. (2010) Quantitative textural analysis of igneous
1016 rocks and the kinetics and dynamics of magma solidification processes. *Earth
1017 Science Frontiers*, 17, 246–266.
- 1018 Yu, S., Zhang, J., Qin, H., Sun, D., Zhao, X., Cong, F. and Li, Y. (2015) Petrogenesis of
1019 the early Paleozoic low-Mg and high-Mg adakitic rocks in the North Qilian
1020 orogenic belt, NW China: Implications for transition from crustal thickening to
1021 extension thinning. *Journal of Asian Earth Sciences*, 107, 122–139.
- 1022 Zeng, L., Zhang, K., Tang, X., Zhang, Y. and Li, Z. (2018) Mid-Permian rifting in
1023 Central China: Record of geochronology, geochemistry and Sr–Nd–Hf isotopes of
1024 bimodal magmatism on NE Qinghai–Tibetan Plateau. *Gondwana Research*, 57,
1025 77–89.

- 1026 Zhan, Q.Y., Zhu, D.C., Wang, Q., Weinberg, R.F., Xie, J.C., Li, S.M., Zhang, L.L. and
1027 Zhao, Z.D. (2020) Source and pressure effects in the genesis of the Late Triassic
1028 high Sr/Y granites from the Songpan-Ganzi Fold Belt, eastern Tibetan Plateau.
1029 *Lithos*, 368, 105584.
- 1030 Zhang, Y.Z., Wang, X.L., Li, J.Y., He, Z.Y., Zhang, F.F., Chen, X., Wang, S., Du, D.H.,
1031 Huang, Y. and Jiang, C.H. (2021) Oligocene Leucogranites of the Gangdese
1032 Batholith, Southern Tibet: Fractional Crystallization of Felsic Melts from Juvenile
1033 Lower Crust. *Journal of Petrology*, 62, egab076.
- 1034 Zheng, J.P., Griffin, W.L., Sun, M., O'Reilly, S.Y., Zhang, H.F., Zhou, H.W., Xiao, L.,
1035 Tang, H.Y. and Zhang, Z.H. (2010) Tectonic affinity of the west Qinling terrane
1036 (central China): North China or Yangtze? *Tectonics*, 29.
- 1037 Zhou, J., Wang, Q., Wyman, D.A. and Zhao, Z. (2020) Petrologic reconstruction of the
1038 Tieshan magma plumbing system: Implications for the genesis of magmatic-
1039 hydrothermal ore deposits within originally water-poor magmatic systems. *Journal*
1040 *of Petrology*, 61, egaa056.
- 1041
- 1042

1043

Figure and Table Captions

1044 **Fig. 1.** (a) Simplified geological map of China, showing the major tectonic units
1045 (after Zheng et al., 2010). (b) Geological map of the West Qinling Orogenic Belt,
1046 showing the distribution of Early Mesozoic granitoids (after Hu et al., 2019; Li et al.,
1047 2015; Luo et al., 2012; Xing et al., 2020; Zeng et al., 2018). Data sources for the zircon
1048 U–Pb ages are given in Table DR1. Place names: WQ, West Qinling; SG, Songpan–
1049 Garzê Terrane; QD, Qaidam; QL, Qilian Terrane; NQ, North Qinling; YB, Yangtze
1050 Block; NCB, North China Block; SCS, South China Sea; QT, Qiangtang Terrane; LT,
1051 Lhasa Terrane; CB, Cathaysia Block.

1052 **Fig. 2.** The geological sketch map of the Zhuyuan pluton

1053 **Fig. 3.** Representative field and microstructural photographs of the Zhuyuan pluton.
1054 (a) Photograph of the Zhuyuan granodiorites; (b) Plagioclases with polysynthetic
1055 twinning; (c) A plagioclase phenocryst with a sieve texture; (d) A plagioclase
1056 phenocryst with oscillatory zoning; (e) A clinopyroxene crystal enclosed by amphibole;
1057 (f) A clinopyroxene crystal enclosed by amphibole and biotite; (g) A clinopyroxene
1058 crystal with clear core–rim texture; (h) An orthopyroxene crystal enclosed by
1059 amphibole; (i) An unzoned orthopyroxene (black outline) mantled by amphibole.
1060 Mineral abbreviations: Cpx, clinopyroxene; Opx, orthopyroxene; Amp, amphibole; Bt,
1061 biotite; Pl, plagioclase; Kf, K-feldspar; Qtz, quartz.

1062 **Fig. 4.** Classification diagrams for rock-forming minerals from the granodiorites of
1063 the Zhuyuan pluton. (a) Wo–En–Fs ternary diagram for pyroxenes (after Morimoto et
1064 al., 1988); (b) Mg/(Mg + Fe²⁺) versus Si diagram for amphiboles (after Leake et al.,

1065 1997); (c) Ternary Mg–(Fe²⁺ + Mn)–(Al^{VI} + Fe³⁺ + Ti) (apfu) diagram for biotite (after
1066 Foster, 1960); (d) Ternary 10 × TiO₂–(FeO^T + MnO)–MgO (wt.%) diagram for biotite
1067 (after Nachit et al., 2005); (e) Or–Ab–An ternary diagram for feldspars (after Smith,
1068 1974). Abbreviation: Cpx, clinopyroxene; Opx, orthopyroxene; Abbreviation: Ab,
1069 albite; Or, orthoclase; An, anorthite; Pl, plagioclase; Amp, amphibole; Bt, biotite; Kf,
1070 K-feldspar.

1071 **Fig. 5.** Back scattered electron images and X_{Mg} and An contents for selected
1072 clinopyroxenes and plagioclases, respectively. (a) and (b) Optically unzoned
1073 clinopyroxenes (ZY17-11-2 and ZY17-13-2); (c) and (d) A normally zoned
1074 clinopyroxene and the core–rim profile of its X_{Mg} (ZY17-4-3); (e) and (f) A reversely
1075 zoned clinopyroxene and the core–rim profile of its X_{Mg} (ZY17-4-2); (g) A plagioclase
1076 crystal with a sieve texture (ZY17-4-1); (h) A plagioclase crystal without sieve texture
1077 (ZY17-6-1). Mineral abbreviations: Cpx, clinopyroxene; Opx, orthopyroxene; Pl,
1078 plagioclase; Amp, amphibole; Bt, biotite.

1079 **Fig. 6.** (a, c, e, g) Chondrite-normalized REE patterns and (b, d, f, h) primitive
1080 mantle-normalized trace element patterns for clinopyroxene and amphibole from the
1081 Zhuyuan pluton. The normalization values are from Sun and McDonough (1989).

1082 **Fig. 7.** Back scattered electron image and LA-ICP-MS maps of representative
1083 elements and important parameters for a reversely zoned clinopyroxene from sample
1084 ZY17-4. All LA-ICP-MS maps show probability density abundances to accentuate
1085 distribution characteristics. LA-ICP-MS data of Profile A extracted parallel to line A–
1086 B are listed in Table DR4.

1087 **Fig. 8.** Back scattered electron image and LA-ICP-MS maps of representative
1088 elements and important parameters for an orthopyroxene + amphibole assemblage from
1089 sample ZY17-15. All LA-ICP-MS maps show probability density abundances to
1090 accentuate distribution characteristics.

1091 **Fig. 9.** Back scattered electron image and LA-ICP-MS maps of representative
1092 elements and important parameters for a biotite from sample ZY17-4. All LA-ICP-MS
1093 maps show probability density abundances to accentuate distribution characteristics.
1094 LA-ICP-MS data of Profile B extracted parallel to line C–D are listed in Table DR4.

1095 **Fig. 10.** (a) and (b) Amphiboles outlined in photomicrographs of samples ZY17-1
1096 and ZY17-11, respectively; (c) and (d) The CSD diagrams of $\ln(n)$ versus size of
1097 amphibole for samples ZY17-1 and ZY17-11, respectively, where ‘n’ represents the
1098 number of grains. Slope and intercept definitions are as follows: Slope = $-1/Gt$;
1099 Intercept = I/G , where nucleation rates (I) and crystal residence reservoir (t) were
1100 calculated by assuming a constant crystal growth rate (G; Marsh, 1988).

1101 **Fig. 11.** Chondrite-normalized REE distribution patterns for melts in equilibrium
1102 with (a) unzoned clinopyroxenes (Type-1 Cpx); (b) normally zoned clinopyroxenes
1103 (Type-2 Cpx); (c) reversely zoned clinopyroxenes (Type-3 Cpx); (d) amphiboles
1104 (Amp); The normalization values are from Sun and McDonough (1989).

1105 **Fig. 12.** Sr/Y values of different minerals versus the Sr/Y values of the melts in
1106 equilibrium with them (a), and the melts with Sr/Y values higher than 30 are considered
1107 to have high Sr/Y signature; Ce/Pb values of different minerals versus the Ce/Pb values
1108 of the melts in equilibrium with them (b). The Ce/Pb value of mantle derived melt is

1109 generally greater than 9, while that of shell derived melt is usually less than 4 (Hofmann
1110 et al., 1986; Sims and DePaolo, 1997).

1111 **Fig. 13.** Schematic diagram showing the hypothetical magma conduit system used
1112 by magmas that formed the Zhuyuan adakitic granodiorites and the various possible
1113 mineral crystallization environments. See text for a detailed discussion.

1114 **Fig.14.** Chondrite normalized REE patterns of calculated intermediate felsic sources
1115 (color lines) of the high Sr/Y undiluted melt of the Zhuyuan granodiorites under
1116 different conditions. Each color line corresponds to different experiments listed in
1117 Table DR7. The source rocks corresponding to Exp 1 to 4 are garnet-bearing semi-
1118 pelitic metasedimentary gneiss, orthogneiss, garnet-bearing metasedimentary gneiss
1119 and biotite tonalite

1120

1121 **Table.1.** The important parameters of rock-forming minerals of the Zhuyuan
1122 granodiorites

1123 **Table 2.** The important parameters of the melts in equilibrium with rock-forming
1124 minerals from the Zhuyuan granodiorites

1125 **Table 3.** Crystallization conditions of amphibole and clinopyroxene from the
1126 Zhuyuan granodiorites

1127

1128 **Electronic Supplementary materials**

1129 **Supplementary Table DR1.** Compilation of previously published zircon U–Pb ages
1130 of the Triassic igneous activity in the Western Qinling Orogen

1131 **Supplementary Table DR2.** Compilation of whole-rock geochemical data and Ti-
1132 in zircon thermometer data for the Zhuyuan granodiorites

1133 **Supplementary Table DR3.** Electron microprobe analysis results of rock-forming
1134 minerals from the Zhuyuan granodiorites and standard materials of the Astimex series

1135 **Supplementary Table DR4.** LA-ICP-MS results of rock-forming minerals from
1136 the Zhuyuan granodiorites and standard materials

1137 **Supplementary Table DR5.** Textual parameters of amphibole in the samples from
1138 the Zhuyuan pluton in West Qinling

1139 **Supplementary Table DR6.** Calculated compositions of the melts in equilibrium
1140 with rock-forming minerals from the Zhuyuan granodiorites and the partition
1141 coefficients used

1142 **Supplementary Table DR7.** Modeled compositions of the "undiluted melts" and
1143 source rocks

1144

1145 **Supplementary Figure DR1.** Classification diagrams for the granodiorites from the
1146 Zhuyuan pluton. (a) Q-A-P diagram (after Streckeisen, 1976); I-Quartzolite; II-
1147 Quartz-rich granitoid; III-Alkali-feldspar granite; IV-Syenogranite; V-Monzogranite;
1148 VI-Granodiorite; VII-Tonalite; VIII-Alkali-feldspar quartz syenite; IX-Quartz
1149 syenite; X-Quartz monzonite; XI-Quartz monzodiorite/monzogabbro; XII-Quartz
1150 diorite/Quartz gabbro; XIII-Alkali-feldspar syenite; XIV-Syenite; XV-Monzonite;
1151 XVI-Monzodiorite/Monzogabbro; XVII-Diorite/Gabbro.

1152 **Supplementary Figure DR2.** (a) $(Dy/Yb)_N$ versus $(La/Yb)_N$ diagram (after He et al.,
1153 2011) for adakite-like rocks from the Zhuyuan pluton. (b) La/Sm versus La/Nb diagram
1154 for adakitic rocks from the Zhuyuan pluton.

1155

1156 **Other Supplementary Materials**

1157 Description of **GEOLOGICAL SETTING**

1158 Description of **ANALYTICAL METHODS**

1159 Description of the **RESULTS** of “**Whole-rock major and trace element**
1160 **geochemistry**”

1161 **DISCUSSION** on “**The critical role of magma mixing and antecryst recycling**”

Table.1. The important parameters of rock-forming minerals of the Zhuyuan granodiorites

Mineral	X _{Mg}	An/Or	Sr (ppm)	Y (ppm)	Rb (ppm)	Sr/Y	∑REE (ppm)	Texture	Type
Type-1A Cpx	72.6–81.7	—	34.4–45.5	20.1–24.4	2.69	1.41–2.26	54.3–75.0	poikilitic texture,	antecrysts
Type-1B Cpx	70.0–76.5	—	32.8–38.2	43.3–53.3	0.90–2.03	0.61–0.80	135–189	non-zoned	antecrysts
Type-2 Cpx core	76.1–80.9	—	50.9–52.2	13.8–14.5	0.20–0.36	3.51–3.79	53.7–60.9	poikilitic texture,	antecrysts
Type-2 Cpx rim	71.5–76.2	—	29.3–42.7	29.7–47.7	0.91–2.62	0.61–1.22	139–245	normally zoned	antecrysts
Type-3 Cpx core	74.3–83.2	—	43.1–127	7.57–8.96	0.31–11.7	5.30–14.8	51.0–68.6	poikilitic texture,	antecrysts
Type-3 Cpx rim	75.5–86.9	—	82.5–91.9	6.27–7.57	0.24–0.55	11.7–13.2	37.8–46.6	reversely zoned	antecrysts
Orthopyroxene	80.9–82.8	—	0.29–0.84	1.29–3.77	0.10–0.22	0.45–0.65	0.72–2.82	poikilitic texture	antecrysts
Amphibole	63.1–74.6	—	17.0–29.8	58.2–141	1.54–1.94	0.15–0.33	303–693	disequilibrium boundary texture	antecrysts
Type-1 Pl	—	An: 32.9–51.6	965–1519	0.14–0.21	10.4–318	6002–9768	12.8–45.3	sieve texture	antecrysts
Type-2 Pl	—	An: 14.9–29.4	865–1494	0.10–0.22	0.31–4.28	4254–14513	15.3–36.2	non-sieve texture	orthocrysts
Biotite	54.4–61.5	—	1.74–6.74	0.15–0.33	317–601	17.5–43.8	0.30–4.12	interstitial mineral	orthocrysts
K-feldspar	—	Or: 72.4–95.8	535–1029	< 0.1	197–338	> 5345	1.47–16.1	interstitial mineral	orthocrysts

Table 2. The important parameters of the melts in equilibrium with rock-forming minerals from the Zhuyuan granodiorites

Equilibrium melt	Mg#	Cr (ppm)	Ni (ppm)	Eu/Eu*	Sr/Y	Sr/Rb	Sr/Ba	Ce/Pb	Environment
Type-1A Cpx	39.5–47.7	46.5–71.2	28.1–46.0	0.54–0.68	4.52–7.27	—	—	42.5–125	A
Type-1B Cpx	42.7–55.5	145–272	92.4–93.5	0.41–0.43	1.97–2.57	—	—	78.8–156	
Type-2 Cpx core	47.2–54.2	318–362	31.9–33.3	0.72–0.77	11.3–12.2	—	—	11.6–19.4	B
Type-2 Cpx rim	41.3–47.3	101–460	34.6–67.7	0.32–0.46	1.97–3.93	—	—	41.2–133	
Type-3 Cpx core	44.7–58.1	38.2–244	45.8–85.1	0.82–0.96	17.0–47.6	—	—	23.9–55.7	C
Type-3 Cpx rim	48.4–65.0	916–1532	122–173	0.85–1.02	37.6–42.4	—	—	5.07–25.5	
Orthopyroxene	56.8–59.9	976–1190	169–239	—	11.7–21.8	—	—	~11.4	D
Amphibole	21.7–34.6	—	—	0.13–0.29	4.13–21.6	—	—	4.4–18.9	E
Type-1 Pl	—	—	—	15.9–23.3	218–315	0.20–6.81	0.40–1.27	3.18–5.59	F
Type-2 Pl	—	—	—	14.6–67.4	96.5–376	26.4–252	0.99–1.67	1.55–2.27	G
Biotite	—	—	—	—	49.5–124	—	—	0.01–0.07	H
K-feldspar	—	—	—	—	>>29	—	—	0.05–0.84	

Table 3. Crystallization conditions of amphibole and clinopyroxene from the Zhuyuan granodiorites

Mineral	Temperature °C	Pressure GPa	Depth km
Type-1 Cpx	1150–1191	0.48–0.75	18.1–28.4
Type-2 Cpx	1130–1192	0.40–0.84	15.3–31.7
Type-3 Cpx	1173–1211	0.38–0.61	14.2–23.0
Amphibole	744–814	0.20–0.35	7.64–13.4

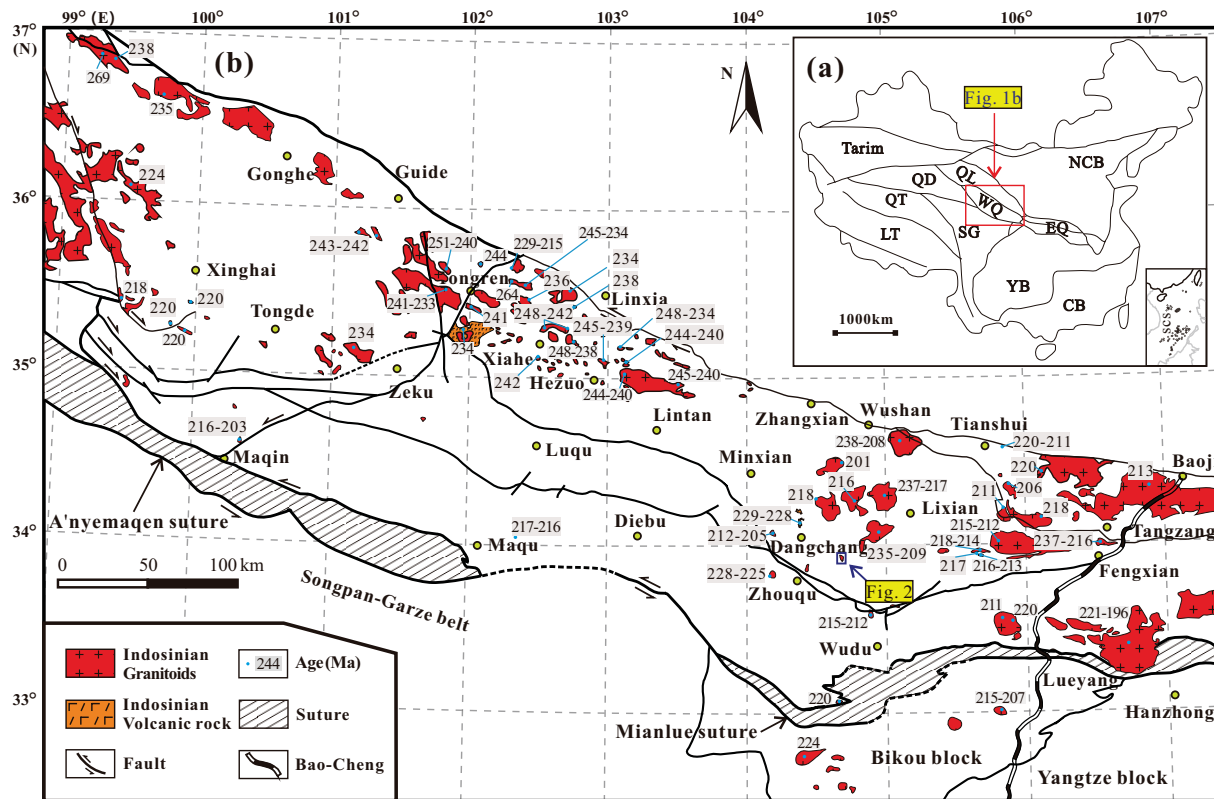


Figure 1

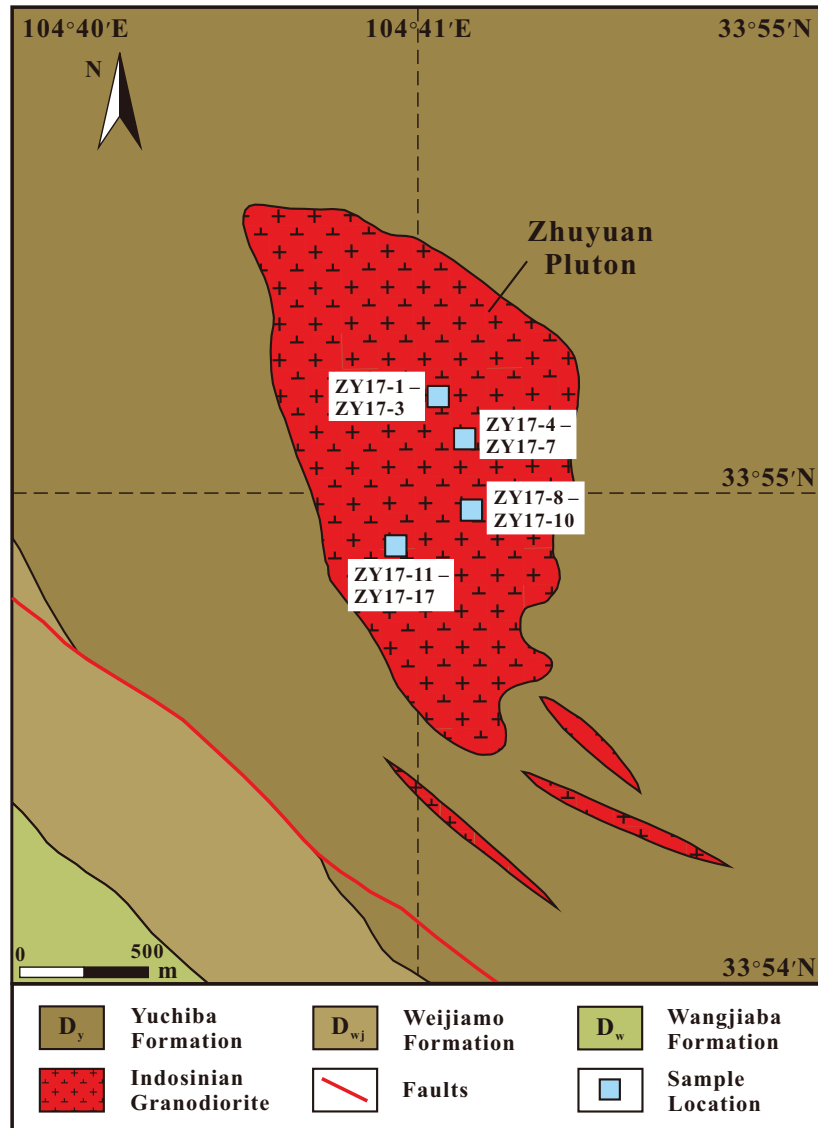


Figure 2

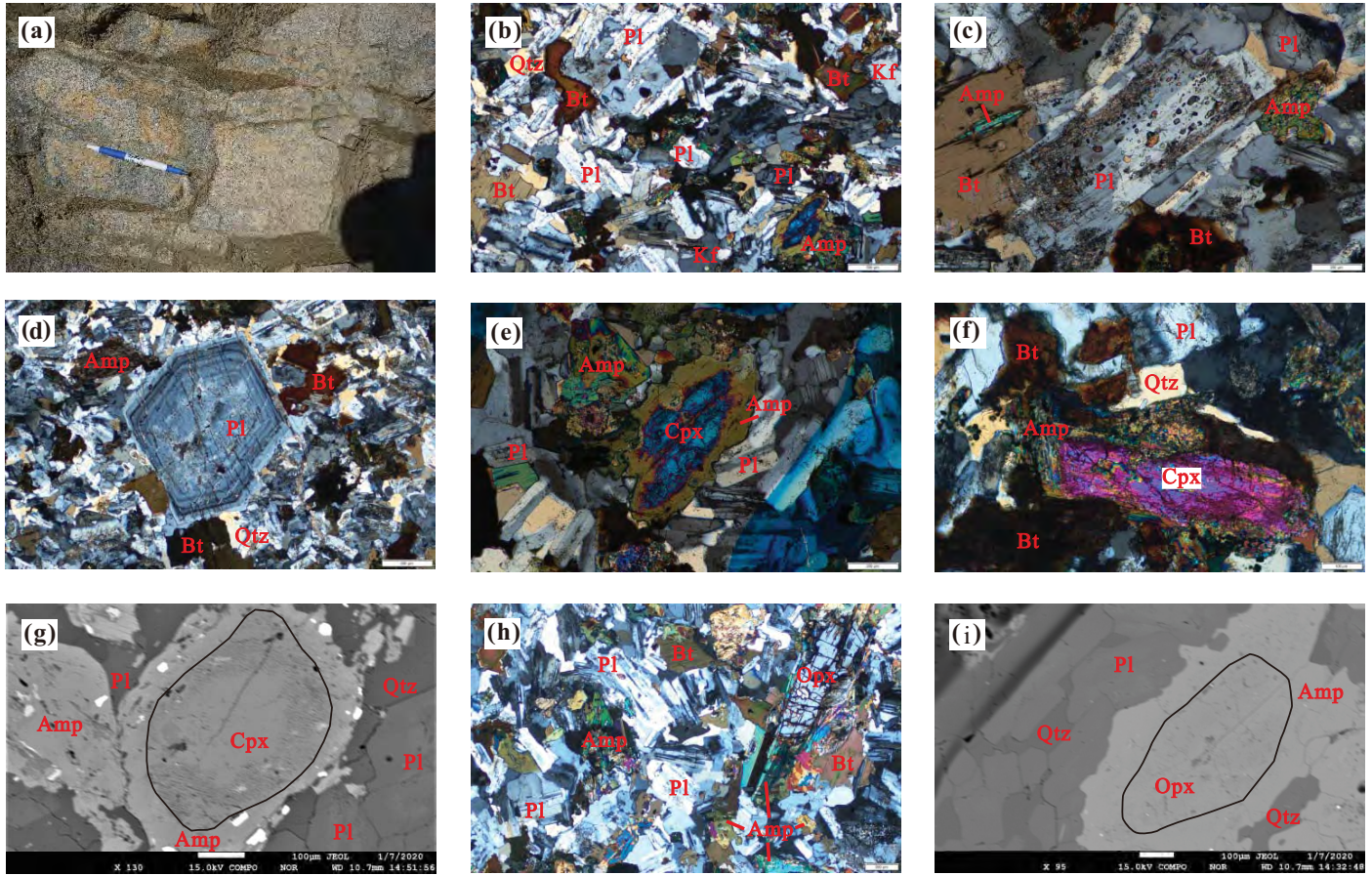


Figure 3

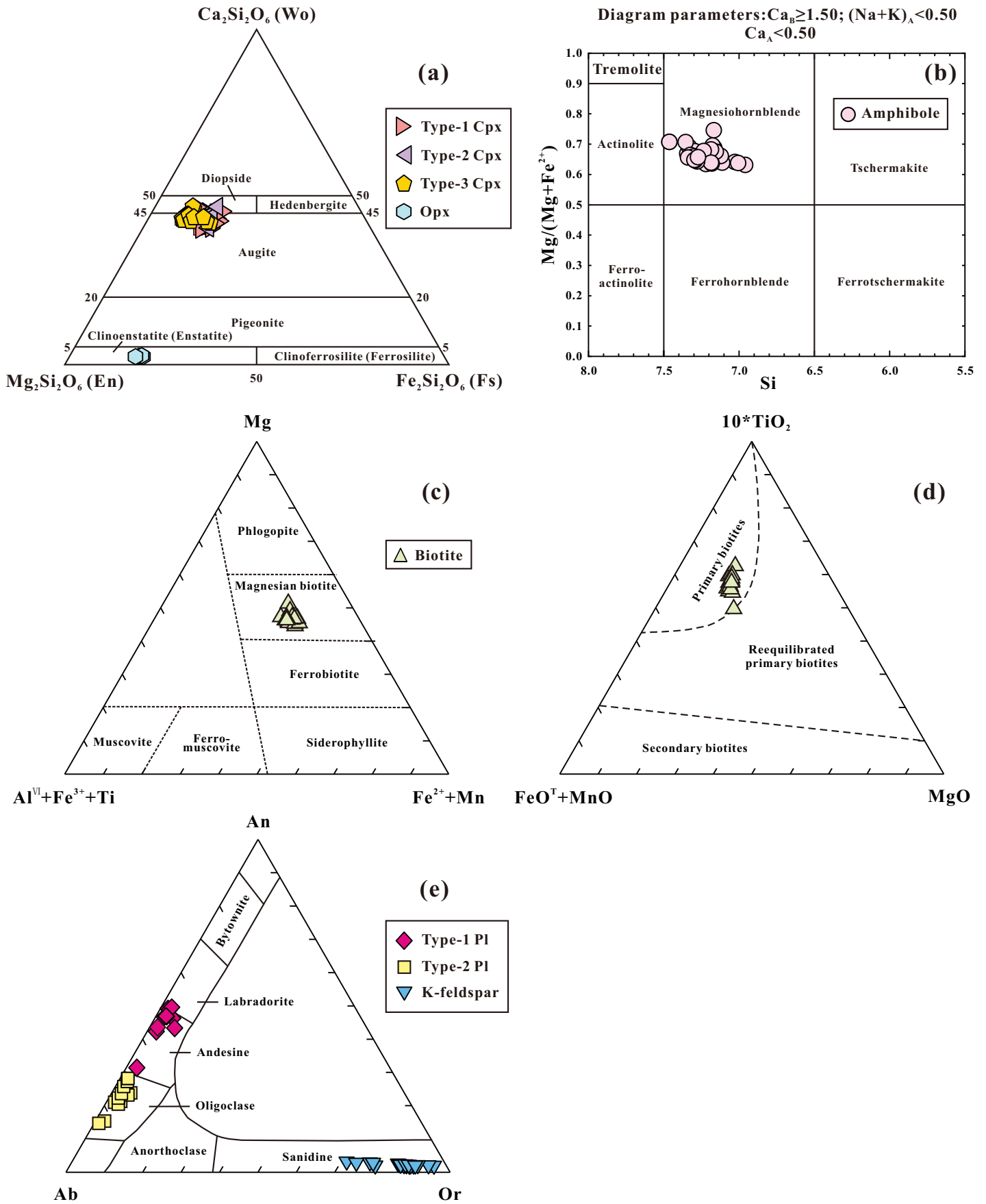


Figure 4

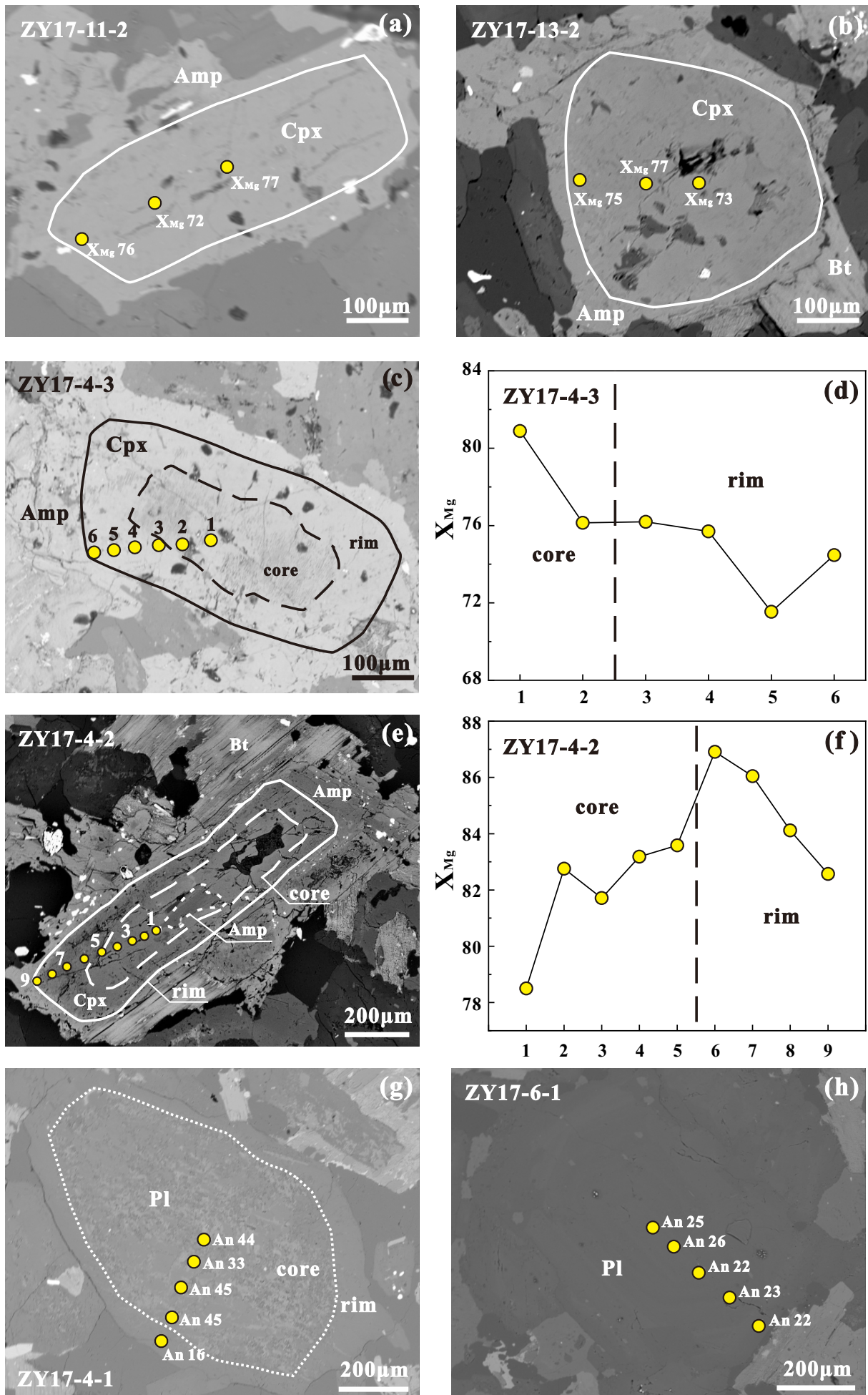


Figure 5

Always consult and cite the final, published document. See <http://www.minsocam.org> or GeoscienceWorld

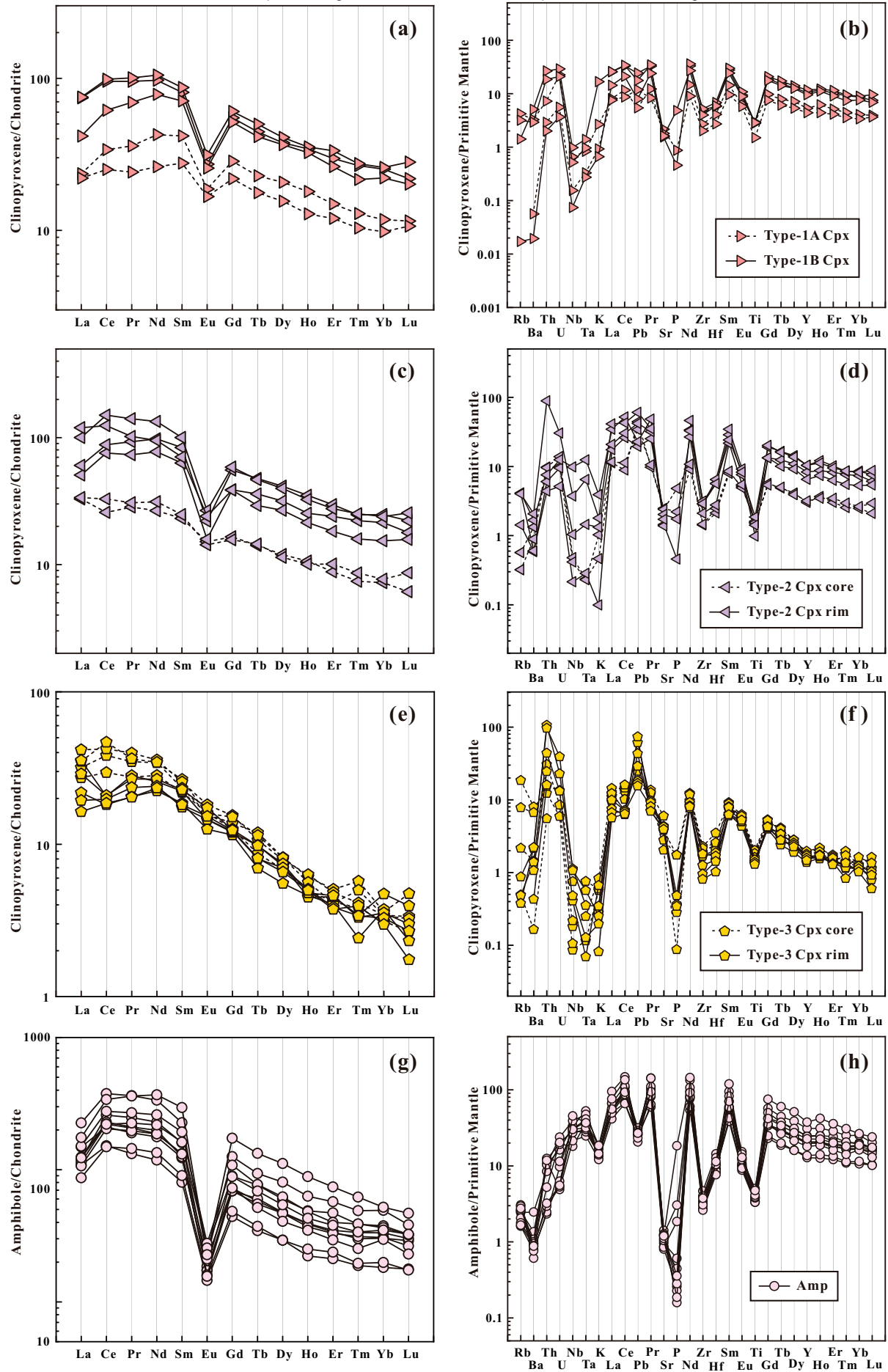


Figure 6

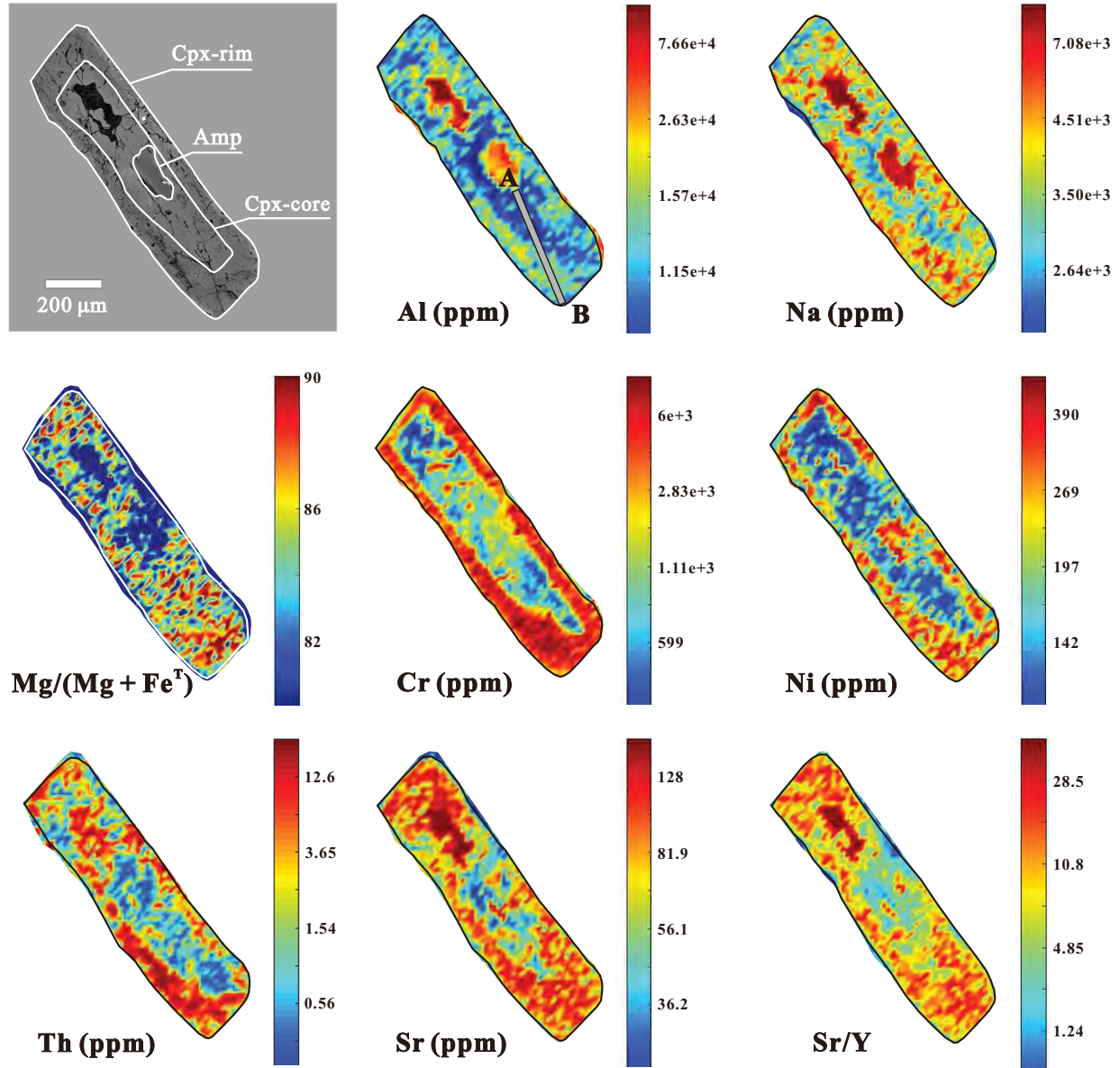


Figure 7

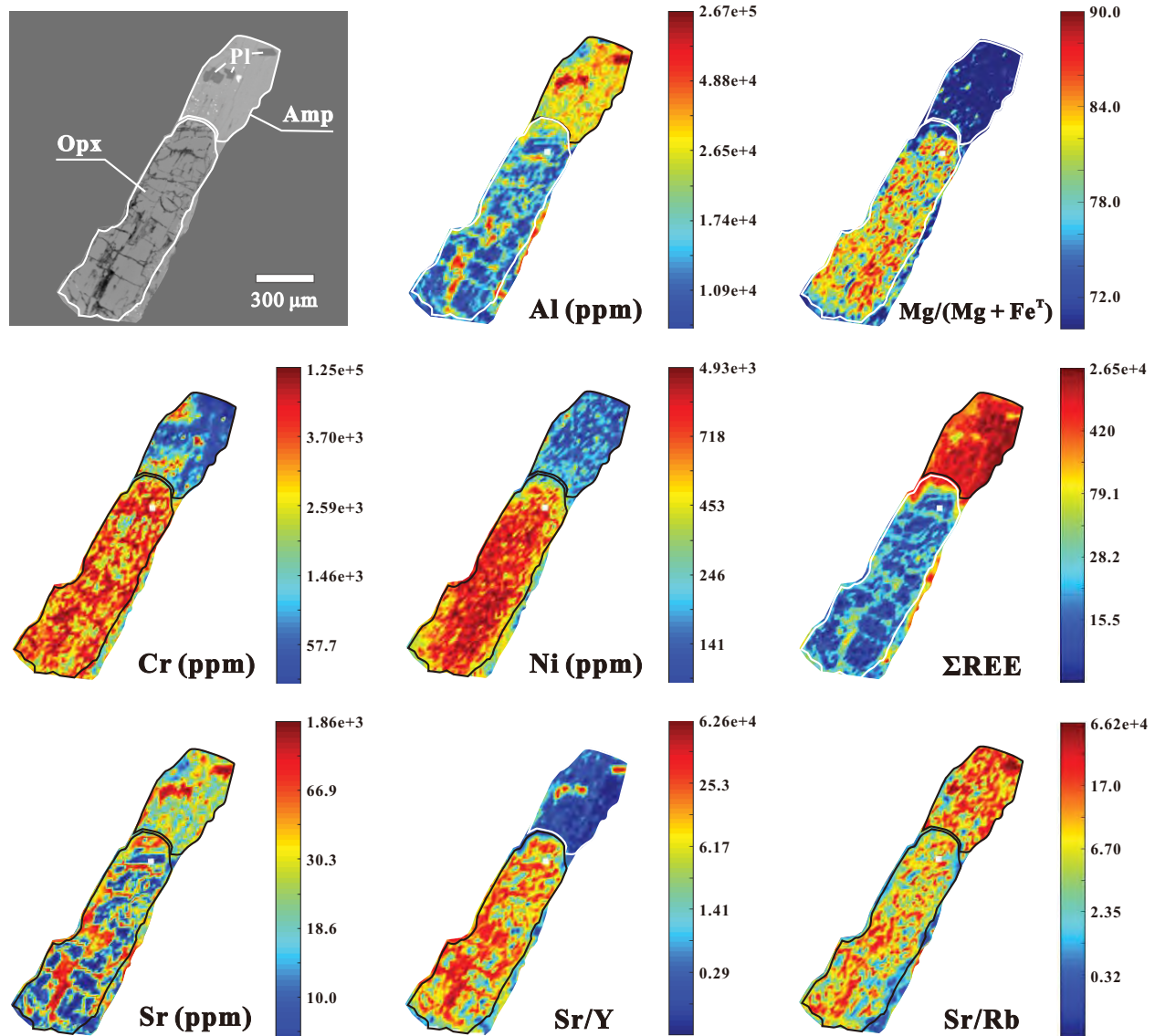


Figure 8

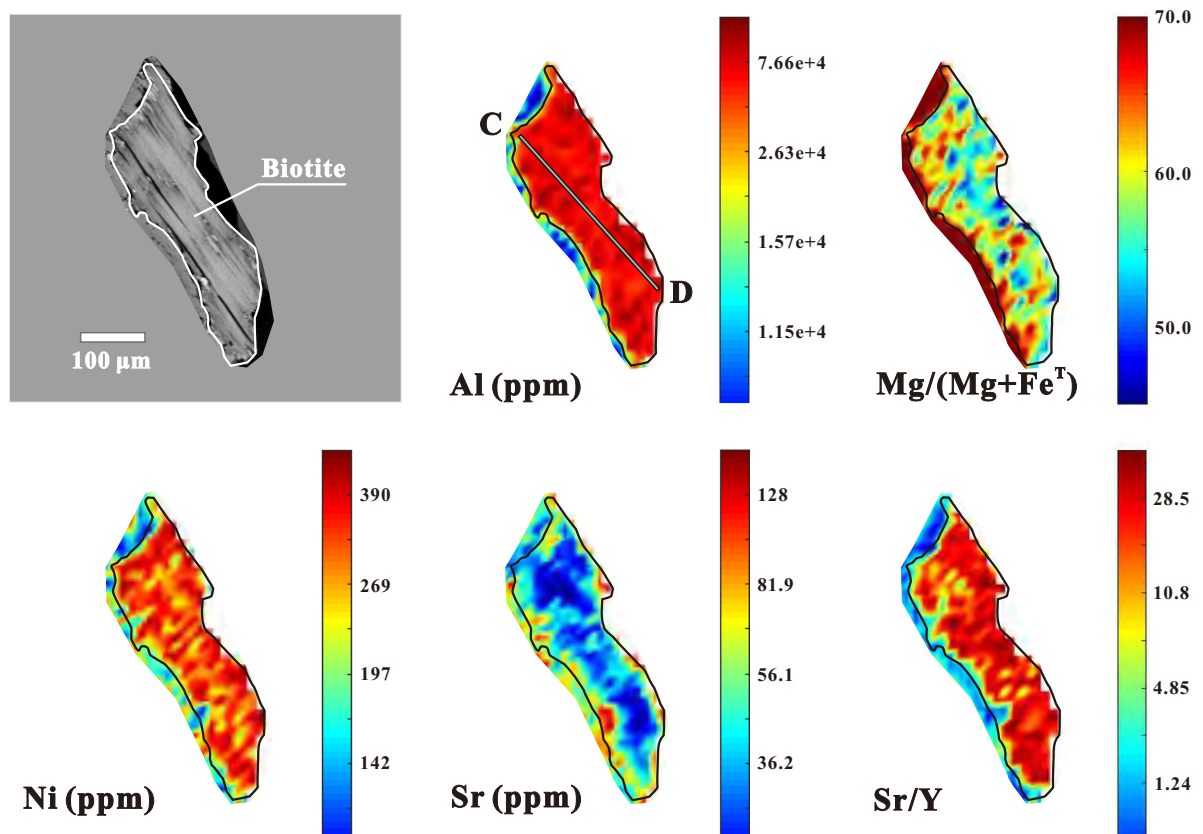


Figure 9

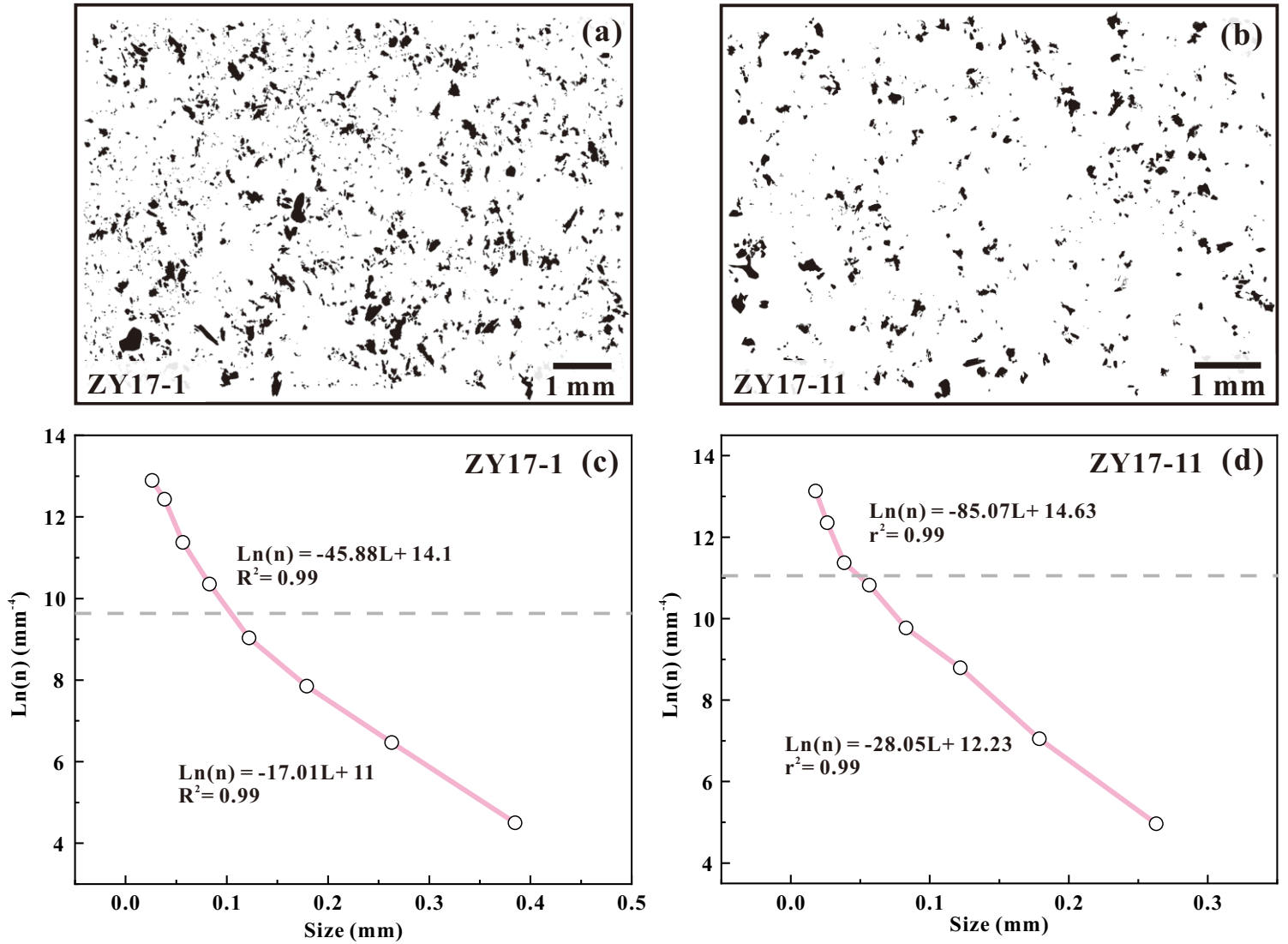


Figure 10

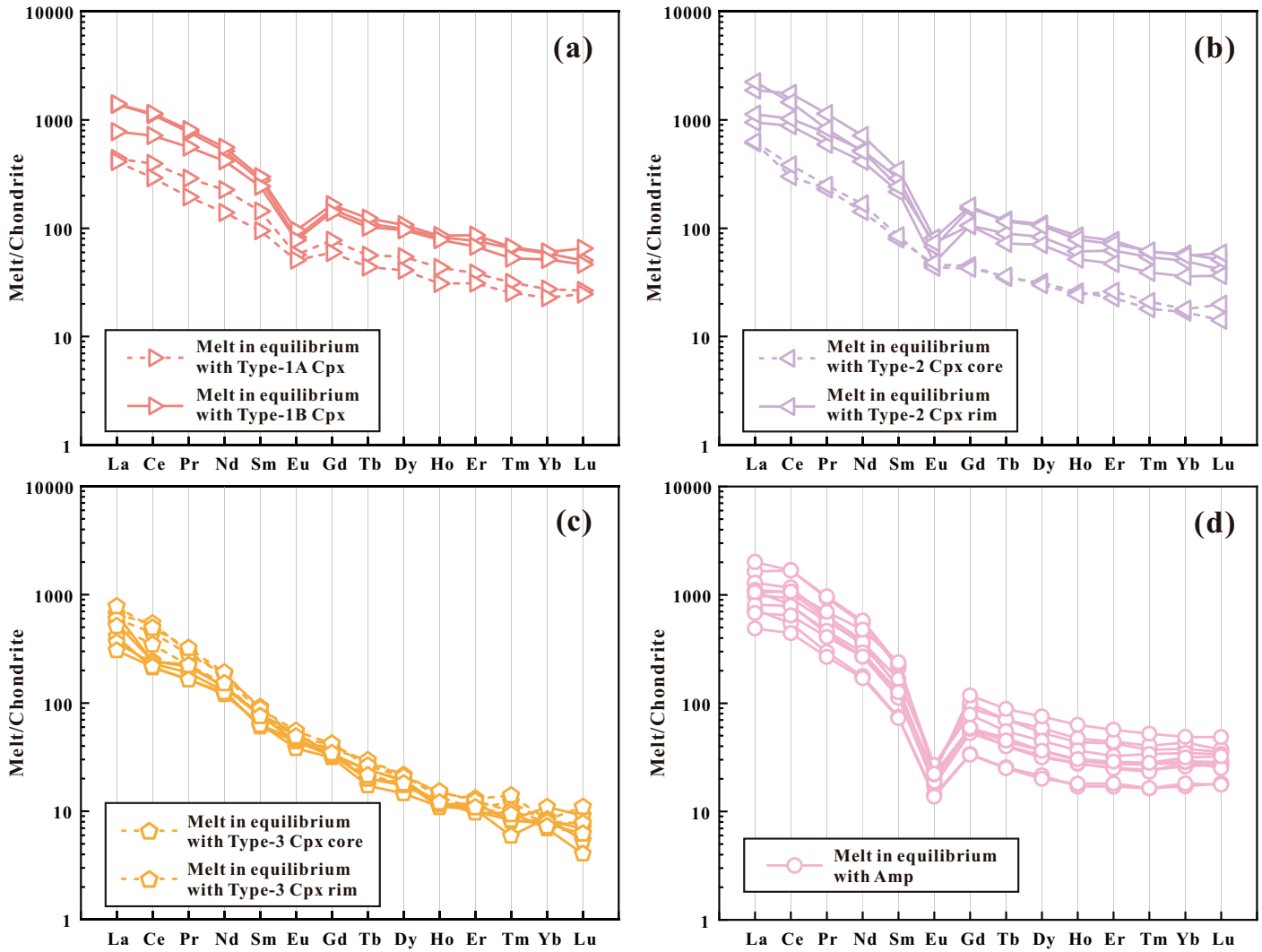


Figure 11

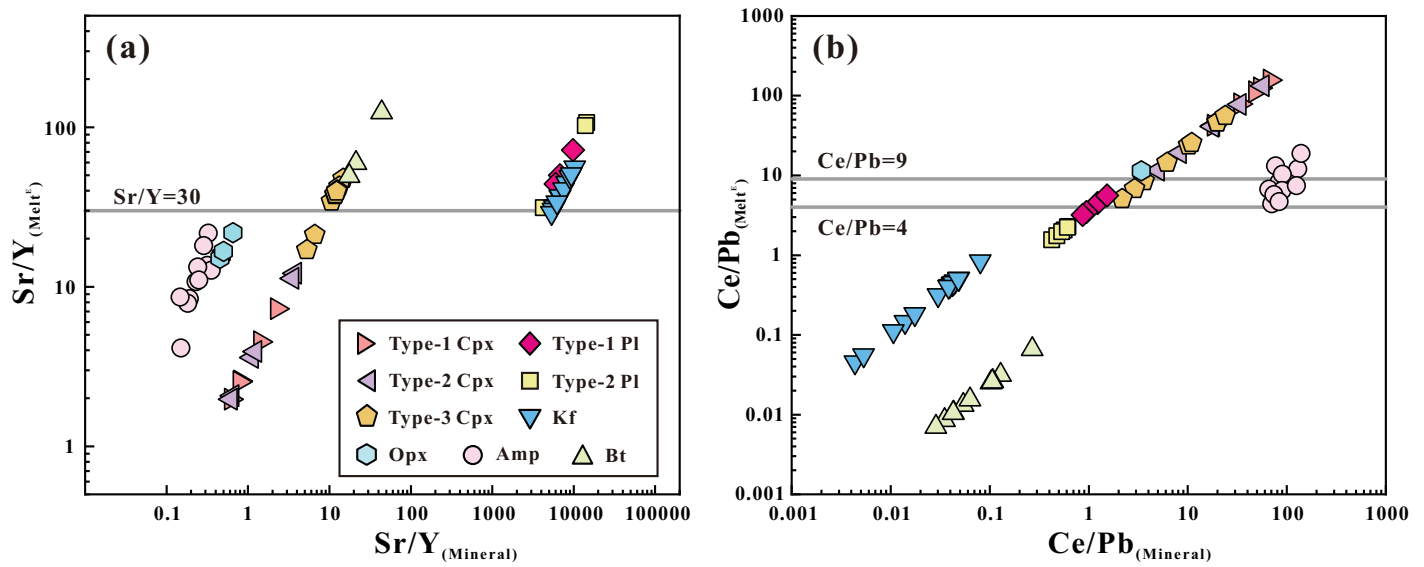


Figure 12

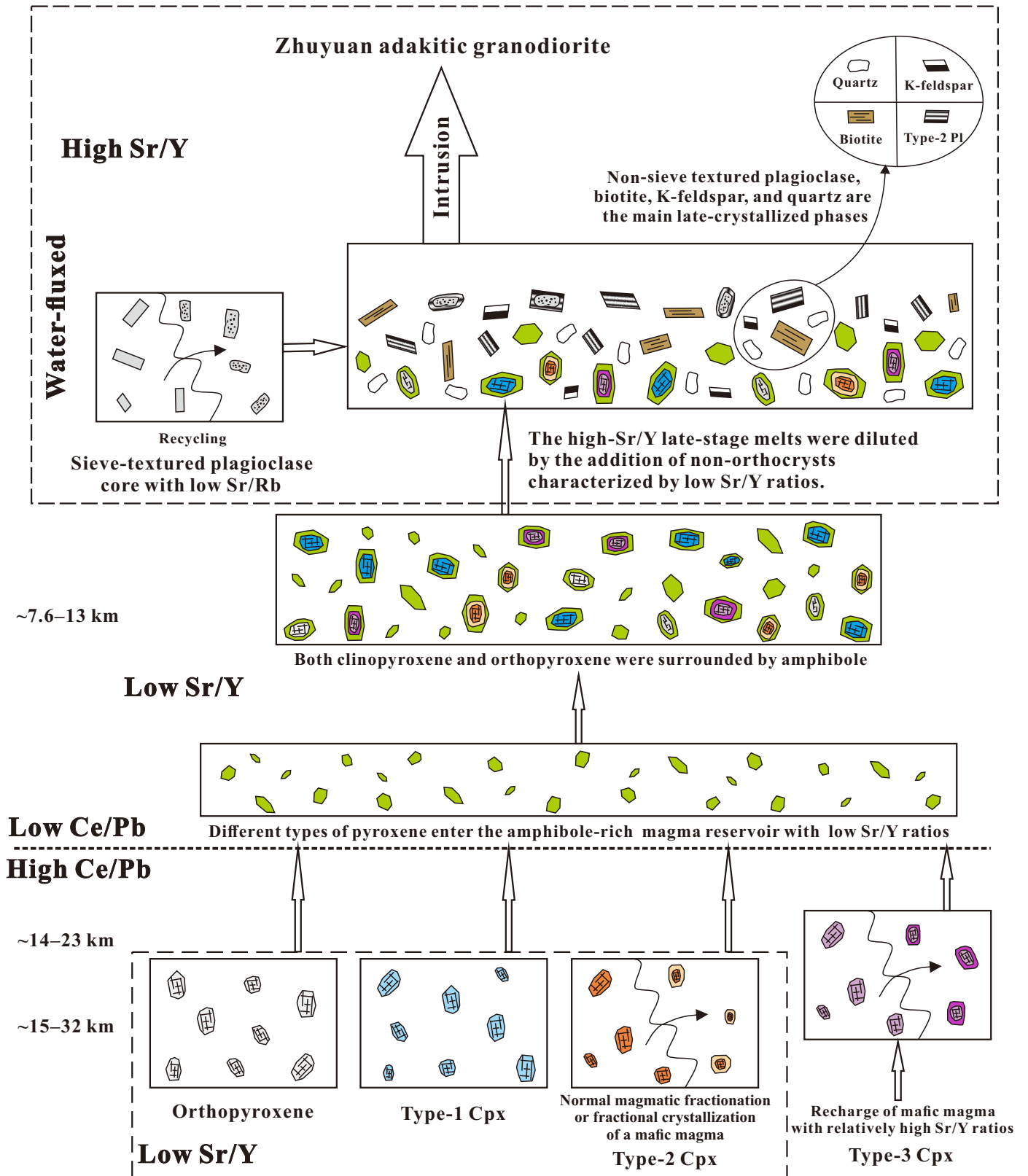


Figure 13

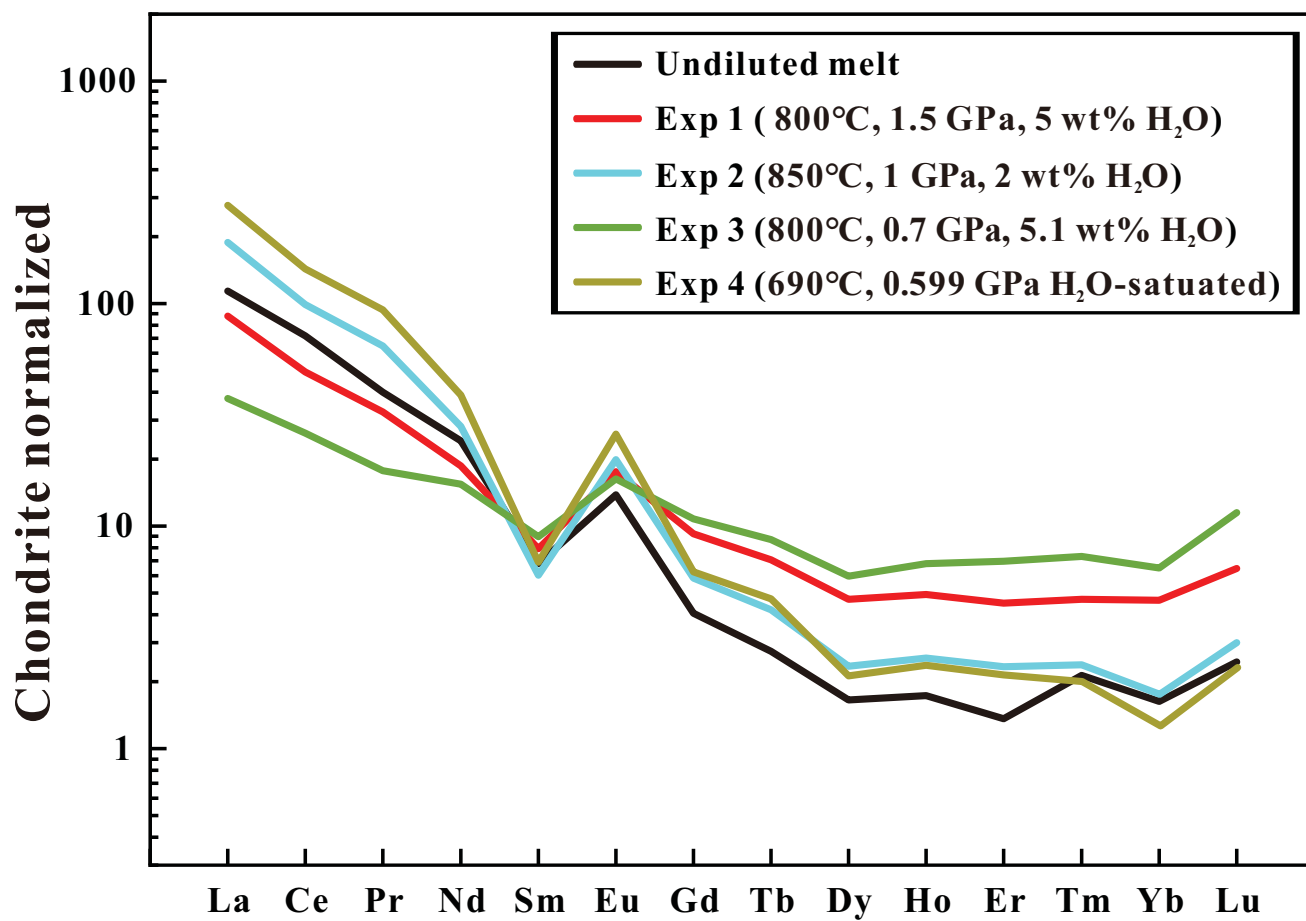


Figure 14